Synchronous N-S and E-W extension at the Tibet-to-Himalaya transition in NW Bhutan

F. J. Cooper[1,2], K. V. Hodges[2], R. R. Parrish[3], N. M. W. Roberts[3], and M. S. A. Horstwood[3]

[1]Now at School of Earth Sciences, University of Bristol, Bristol, UK, [2]School of Earth and Space Exploration, Arizona State University, Tempe, Arizona, USA, [3]NERC Isotope Geosciences Laboratory, British Geological Survey, Keyworth, UK

Abstract Despite ~50 Myr of continuous continent-continent collision, contractional structures in the Himalayan-Tibetan orogen are today limited to the northern and southern margins of the system, while extension dominates much of the interior. On the Tibetan Plateau, Cenozoic E-W extension has been accommodated by strike-slip faults and extensional grabens, while N-S extension at the Tibet-to-Himalaya transition has been accommodated by the South Tibetan fault system (STFS). The genetic relationship between N-S and E-W extension is disputed, although age constraints indicate temporal overlap of at least 7 Myr. In NW Bhutan the two intersect where the STFS basal detachment is cut by the Yadong cross structure (YCS), an extensional half graben that provides a rare opportunity to constrain relative timings. We report U-Pb zircon dates from four STFS footwall leucogranites consistent with episodic magmatism during the middle-late Miocene and in situ U(-Th)-Pb monazite and xenotime dates from three metasedimentary rocks ranging from late Oligocene to middle Miocene. We suggest that amphibolite facies footwall metamorphism was ongoing at the time the basal STFS detachment initiated as a ductile structure in the middle-late Miocene. Late-stage granitic intrusions may reflect footwall melting during extensional exhumation along the STFS, but post-metamorphic and post-intrusion fabrics suggest that most displacement occurred after emplacement of the youngest granites. Some of the oldest YCS-related fabrics are found in a deformed 14 Ma leucogranite, implying middle Miocene ductile deformation. This observation, along with evidence for subsequent brittle YCS deformation, suggests that N-S and E-W extensional structures in the area had protracted and overlapping deformation histories.

1. Introduction

The Himalayan-Tibetan orogen is generally regarded as the type example of a collisional mountain belt, with circa 50 Ma of continuous contraction creating a region of unusually thick lithosphere (60–75 km) [*Hauck et al.*, 1998; *Nelson et al.*, 1996; *Tseng et al.*, 2009]. Today, however, upper crustal contractional structures are limited primarily to the northern and southern margins of the system (Figure 1; see caption for references), while the Tibetan Plateau is dominated by strike-slip and high-angle normal faults, typically expressed as orogen-perpendicular, N-S trending extensional grabens [*Armijo et al.*, 1986; *Molnar and Tapponnier*, 1975; *Taylor and Yin*, 2009]. At the southern margin of the plateau, the boundary with the contractional Himalaya is roughly coincident with a family of orogen-parallel, gently north dipping extensional structures known as the South Tibetan fault system (STFS) [*Burchfiel et al.*, 1992]. While these structures are not active today, similar detachments of Plio-Pleistocene age have been mapped near the modern physiographic southern margin of the Tibetan Plateau [*Hurtado et al.*, 2001; *McDermott et al.*, 2013, 2015; *Meyer et al.*, 2006; *Wiesmayr et al.*, 2002].

Near the Himalayan range crest, the STFS marks the structural boundary between predominantly unmetamorphosed hanging wall rocks of the Tibetan sedimentary sequence (TSS) and amphibolite-grade footwall rocks of the Greater Himalayan sequence (GHS), both of which are thought to have derived from the Indian continent prior to collision [*Hodges*, 2000]. The STFS has been interpreted in some previous papers as a decoupling horizon between E-W extension on the Tibetan Plateau and N-S contraction in the Himalaya [*Hodges et al.*, 2001], although the significance of this system in the development of the orogen is disputed. Opposing models suggest that it has either accommodated significant southward extrusion of the metamorphic core of the orogen (the "channel flow" model) [e.g., *Beaumont et al.*, 2001; *Grujic et al.*, 2002; *Hodges et al.*, 2001; *Nelson et al.*, 1996] or forms a passive roof structure above a contractional orogenic wedge (the "critical taper" model) [e.g., *Kohn*, 2008; *Yin*, 2006; *Yin et al.*, 1994]. It has also been proposed that the basal STFS detachment is a back thrust, kinematically linked to the north vergent Great
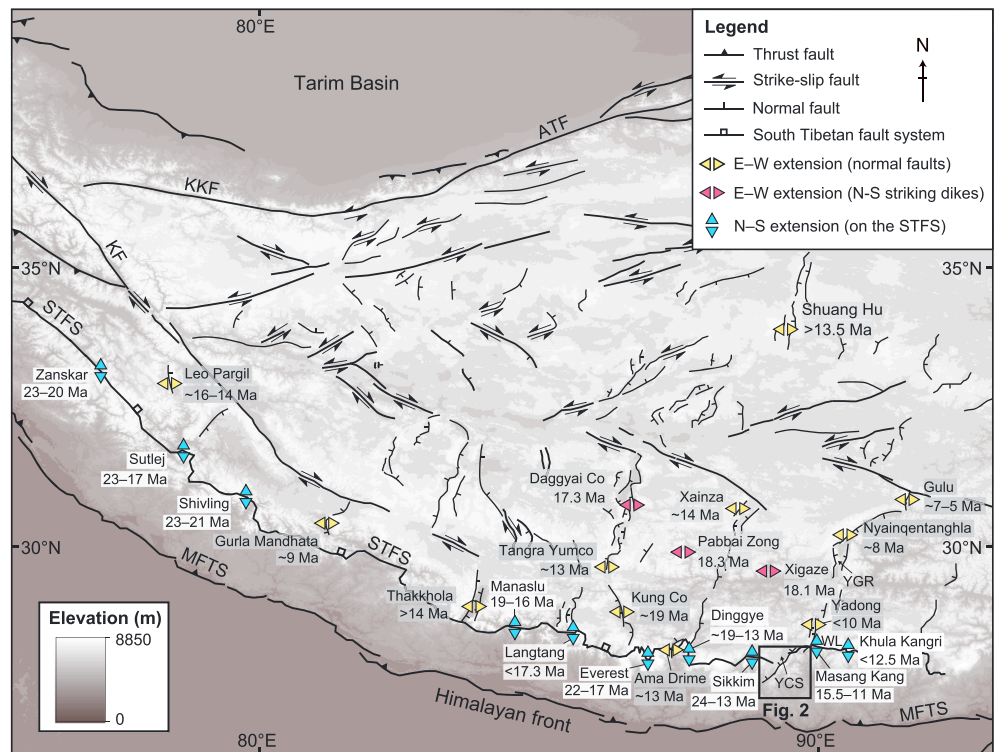
Figure 1. Major fault systems of the Himalayan-Tibetan orogen. Reproduced and modified from *Mitsuishi et al.* [2012] with the kind permission of the authors. Fault systems follow *Hodges* [2000], *Blisniuk et al.* [2001], *Taylor et al.* [2003], *Taylor and Yin* [2009], and *Long et al.* [2011]: STFS = South Tibetan fault system, MFTS = Main Frontal thrust system, KF = Karakoram Fault, WL = Wagye La, YGR = Yadong-Gulu rift, YCS = Yadong cross structure. Triangles denote sites of identified E-W and N-S extension and time of initiation derived from either dike emplacement or fault motion. Dike emplacement: Daggyai Co, Pabbai Zong, and Xigaze, [*Williams et al.*, 2001]. E-W extension on the Tibetan Plateau: Leo Pargil [*Hintersberger et al.*, 2010; *Thiede et al.*, 2006], Gurla Mandhata [*Murphy et al.*, 2002], Thakkhola [*Coleman and Hodges*, 1995], Tangra Yumco [*Dewane et al.*, 2006], Ama Drime [*Cottle et al.*, 2009; *Kali et al.*, 2010], Xainza [*Hager et al.*, 2009], Shuang Hu [*Blisniuk et al.*, 2001], Yadong [*Edwards and Harrison*, 1997], Nyainqentanglha [*Harrison et al.*, 1995a], Gulu [*Stockli et al.*, 2002], and Kung Co [*Mitsuishi et al.*, 2012]. N-S extension related to the STFS: Zanskar [*Walker et al.*, 1999], Sutlej [*Vannay et al.*, 2004], Shivling [*Searle et al.*, 1999], Manaslu [*Guillot et al.*, 1994], Langtang [*Searle et al.*, 1997], Everest [*Hodges et al.*, 1992, 1988; *Murphy and Harrison*, 1999; *Viskupic et al.*, 2005], Dinggye [*Zhang and Guo*, 2007], Sikkim [*Kellett et al.*, 2013], Masang Kang [*Kellett et al.*, 2009], and Khula Kangri [*Edwards and Harrison*, 1997].

Counter thrust system in southern Tibet [*Webb et al.*, 2013, 2007; *Yin*, 2006; *Yin et al.*, 1994, 1999]. However, minimum constraints on STFS displacement of 65–170 km [*Cooper et al.*, 2013, 2012; *Law et al.*, 2011] are inconsistent with the limited displacement expected on such back thrusts.

The cause of E-W extension on the Tibetan Plateau is also disputed and a variety of proposed models include radial thrusting [e.g., *Armijo et al.*, 1986; *Molnar and Lyon-Caen*, 1989; *Seeber and Armbruster*, 1984], oroclinal bending [e.g., *Kapp and Yin*, 2001; *Ratschbacher et al.*, 1994; *Robinson et al.*, 2007], oblique convergence [e.g., *McCaffrey*, 1996; *McCaffrey and Nabelek*, 1998], convective removal of the mantle lithosphere [*England and Houseman*, 1989], and lateral extrusion of the crust away from the locus of collision [*Hintersberger et al.*, 2010; *Mitsuishi et al.*, 2012; *Molnar and Tapponnier*, 1978; *Molnar and Chen*, 1983; *Royden and Burchfiel*, 1987; *Tapponnier et al.*, 1982; *Whipp et al.*, 2014].

Despite the evident importance of both E-W and N-S extension across the Himalayan-Tibetan orogen, the genetic relationship between the two is poorly understood. Age constraints along the ~2000 km length of the STFS suggest that the main phase of activity lasted from circa 23 to 11 Ma, with faulting initiating first in the west and migrating progressively to the east (Figure 1). The best constraints on the latest motion along the STFS come from the ages of deformed granitic intrusions in the STFS footwall (e.g., 13 Ma in northern Sikkim, India [*Kellett et al.*, 2013], 12.5 Ma in the Khula Kangri region, SE Tibet [*Edwards and Harrison*, 1997; *Wu et al.*, 1998], and 11 Ma in the Masang Kang area of Bhutan [*Kellett et al.*, 2009]).

The main phase of E-W extension on the Tibetan Plateau is thought to have lasted from circa 19 Ma until circa 5 Ma and also shows a younging from west to east, mirroring N-S extension on the STFS (Figure 1). Detailed mapping of Quaternary and active faults [*Armijo et al.*, 1986] and more recent observations of offset Quaternary deposits, such as along the Nyönno Ri fault in the Ama Drime Massif, central Himalaya [*Jessup et al.*, 2008], together with earthquake fault plane solutions [e.g., *Andronicos et al.*, 2007; *Molnar and Lyon-Caen*, 1989] and GPS data [e.g., *Gan et al.*, 2007; *Zhang et al.*, 2004] across Tibet, indicate that E-W extension is ongoing.

Collectively, the data imply that N-S and E-W extension might have been contemporaneous for at least 8 Myr during the Miocene, and possibly even longer, suggesting that both may be interrelated responses to large-scale geodynamics. However, despite the apparent overlap in time across the orogenic system, workers invariably presume that, in a single area, the E-W extensional structures are younger. Direct studies in places where N-S and E-W structures interact have yielded contradictory results, some suggesting that E-W extension is younger, some that the two are more or less coeval. For example, in the Kung Co area of southern Tibet, *Mitsuishi et al.* [2012] found that shallow E-W extension on brittle normal faults was coeval with deeper N-S directed ductile flow. On the other hand, in the Ama Drime massif and Gurla Mandhata core complex of the central Himalaya [*Jessup et al.*, 2008; *Murphy*, 2007; *Murphy and Copeland*, 2005; *Murphy et al.*, 2002], and in the NW Indian Himalaya [*Hintersberger et al.*, 2010], younger E-W extensional structures cut and offset the STFS. In the Annapurna area of Nepal, *Hurtado et al.* [2001] identified Quaternary, N-S striking extensional structures that cut older strands of the STFS, but these were themselves truncated by younger, low-angle, top-north oblique-slip faults of similar orientation to the STFS. This implies that there may have been coeval motion of the two, although *McDermott et al.* [2015] suggested that these younger, E-W striking structures are actually younger features unrelated to the Miocene STFS.

Here we contribute to this discourse by reporting the results of a study in NW Bhutan where a NE-SW trending extensional half graben, the Yadong cross structure, cuts a basal detachment of the South Tibetan fault system.

2. Structural Setting

The Yadong cross structure (YCS) marks the southern extent of the Yadong-Gulu rift system, which extends circa 500 km northeast from the Bhutan-Tibet border as a series of active grabens and half grabens (Figure 1) [*Armijo et al.*, 1986; *Ratschbacher et al.*, 2011; *Wu et al.*, 1998; *Wu et al.*, 2011]. Immediately to the southeast of the YCS is the Jomolhari region of NW Bhutan. Mapping of this area by *Cooper et al.* [2012] suggested that it contains one of the largest continuous exposures of the South Tibetan fault system in the Himalaya. In their study, ground-truthed multispectral satellite mapping indicated that the basal STFS detachment in the area has a minimum top-to-the-north displacement of 65 km, placing shallowly north dipping, recumbently folded, locally fossiliferous, marbles of the Tibetan sedimentary sequence on high-grade gneisses, quartzites, and calc-silicates of the Chekha Formation [*Gansser*, 1983; *Jangpangi*, 1974; *Nautiyal et al.*, 1964; *Tangri and Pande*, 1995] and Greater Himalayan sequence [*Bhargava*, 1995; *Davidson et al.*, 1997; *Gansser*, 1983; *Grujic et al.*, 2002; *Hollister and Grujic*, 2006; *Long and McQuarrie*, 2010; *Long et al.*, 2011; *Swapp and Hollister*, 1991] (Figure 2a).

This interpretation is at odds with other workers in the area who show a more continuous region of TSS units and have argued that the contact between the Chekha Formation and the Greater Himalayan sequence defines a second, structurally lower, strand of the STFS [e.g., *Carosi et al.*, 2006; *Grujic et al.*, 2002, 2011; *Kellett et al.*, 2009; *Long et al.*, 2011] (Figure 2b). However, the similarity in lithology, structural style, and peak metamorphic temperature between these two units makes it difficult to conclude that they are separated by a fault with any significant displacement. Therefore, we follow the interpretation of *Cooper et al.* [2013] that together, they make up the STFS footwall.

Throughout this paper, our rationale and conclusions are placed within this context, following the geologic map in Figure 2a. However, we have also included our sample locations in the alternative geologic map in Figure 2b, so that readers can judge the data independently of the preferred geologic interpretation.

Variably deformed leucogranite sills and dikes interpreted to have formed by anatexis of the Greater Himalayan sequence [*Harris and Massey*, 1994; *Le Fort et al.*, 1987] pervasively intrude the footwall
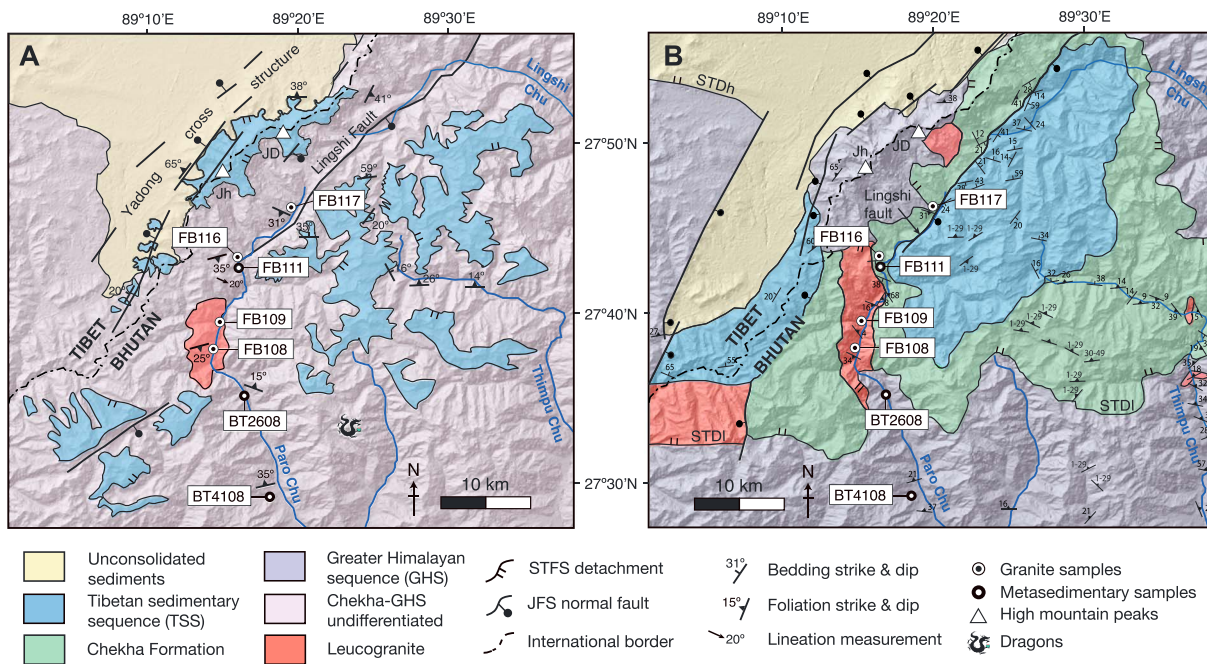
Figure 2. Alternative geological interpretations of the Jomolhari region. (a) Geologic map from *Cooper et al.* [2012], modified in the Mount Jomolhari (Jh)-Mount Jichu Drake (JD) range where the STFS is shown at a higher elevation than previously mapped. In this interpretation, the basal STFS detachment forms a continuous low-angle surface separating isolated erosional remnants of the TSS in its hanging wall from high-grade metamorphic rocks of the Chekha and GHS in its footwall. (b) Geologic map of the same region compiled from *Long et al.* [2011] and *Grujic et al.* [2011] and references therein. In this version, the STFS occurs as two distinct fault strands: a structurally higher, discrete brittle detachment (STDh) and a structurally lower, diffuse ductile shear zone (STDl) interposed by the Chekha Formation, a nonfossiliferous metamorphic unit intruded by leucogranite sills and dikes [*Gansser*, 1983; *Grujic et al.*, 2002; *Kellett et al.*, 2009; *Kellett and Grujic*, 2012]. Following the interpretation in Figure 2a, we treat all of our samples as belonging to the STFS footwall. However, we note that according to the mapping in Figure 2b, samples FB108, FB109, FB111, FB116, and FB117 all lie in the hanging wall to the STDl, though still in the footwall to the STDh.

sequence and a large tourmaline-bearing two-mica leucogranite, the Chung La pluton, lies approximately 20 km south of Mount Jomolhari (Figure 2a). First described and mapped by *Gansser* [1983] and more recently described by *Kellett et al.* [2009] and *Regis et al.* [2014], the full extent of this intrusion is unclear but covers an area of at least 50 km². In Figure 2a, we have followed the original mapping by *Gansser* [1983] but reduced the N-S extent of the intrusion based on our own observations in the field.

The YCS is bound along its eastern margin by the Jomolhari fault system (JFS), a series of west dipping high-angle oblique-slip faults that cut and offset the youngest strands of the STFS. The Jomolhari-Jichu Drake range acts as a rigid horst block within this system, with JFS faulting expressed on its eastern side as a parallel series of high-angle east dipping oblique-slip faults. One of these structures, the Lingshi fault, was first mapped and described by *Gansser* [1983] as "a NE striking structure with a marked upthrow to the NW," and its precise position has been refined in subsequent studies from both field and satellite observations [e.g., *Cooper et al.*, 2012; *Grujic et al.*, 2011; *Kellett and Grujic*, 2012]. *Cooper et al.* [2012] documented a brittle-ductile shear zone of the Lingshi fault striking ENE and dipping 35° to the SSE with a ductile downdip lineation plunging 20° to the ESE, consistent with a top-east normal sense of displacement. Outcrops of the Chung La pluton exhibit a similar micaceous foliation, dipping 25–30° to the SSE, that strengthens progressively from south to north and upsection through the STFS footwall toward the detachment. We interpret this to be an originally STFS-related fabric that has been rotated by slip on the Lingshi fault.

As well as normal-sense displacement on the Lingshi fault, paleomagnetic vertical axis rotations in the Jomolhari region suggest that this structure has accommodated a component of sinistral strike-slip motion since approximately 13 Ma [*Antolín et al.*, 2012]. More recent deformation, evidenced by focal mechanisms of historic earthquakes (e.g., a *M* 5.4 earthquake in 2003) point to it being active as a sinistral strike-slip fault today [*Drukpa et al.*, 2006]. However, the downdip ductile fabric in the Lingshi shear zone and the significant vertical displacement of the Jomolhari-Jichu Drake range, together suggest that dip-slip motion has been a significant and long-lived part of its evolution.

Together, these east and west dipping faults of the JFS create a horst structure along the eastern margin of the YCS that encompasses both Jomolhari and Jichu Drake. This horst block is dominated by STFS footwall rocks of the GHS and Chekha, as shown in previous mapping (Figure 2b), and highlighted by *Regis et al.* [2014], but multispectral satellite data analyzed by *Cooper et al.* [2012] indicate that material shedding from the high peaks along the range contains calcareous lithologies with the same spectral signature as TSS units nearby. In Figure 2a, we place the STFS at a slightly higher elevation in the horst block than *Cooper et al.* [2012], reflecting uplift relative to STFS outcrops to the SE, and follow the interpretation of *Wu et al.* [1998] that the STFS is downdropped to the west across the YCS, buried beneath infilling graben sediments on the Tibetan Plateau.

3. Geochronological Constraints on Extension

Previous geochronologic studies of the STFS footwall in the eastern Himalaya have placed useful constraints on the history of N-S extension there. Th-Pb and U-Pb dating of monazites in STFS-mylonitized granites of the Khula Kangri [*Edwards and Harrison*, 1997] and Wagye La [*Wu et al.*, 1998] regions of southern Tibet (Figure 1) showed that the fault system remained active there until at least approximately 12.5–12 Ma. Across the YCS in Sikkim, India, *Catlos et al.* [2004] obtained Th-Pb zircon and monazite dates from a deformed footwall leucogranite of circa 17 and 15–14 Ma, suggesting continued fault motion until at least 14 Ma. A more recent geochronological study in the same area by *Kellett et al.* [2013] suggested an even more prolonged slip history from at least 23.6 Ma to ~13 Ma. In NW Bhutan, U-Pb and ^{40}Ar/^{39}Ar dating of deformed STFS footwall leucogranites and U-Pb dating of metamorphic monazite in footwall metasediments paints a similar picture, with STFS activity lasting from circa 23 to 11 Ma [*Kellett et al.*, 2009, 2010; *Warren et al.*, 2011]. Analyses of brittle fault surfaces and paleoseismology at the Tibet-to-Himalaya transition in Lunana, ~100 km ENE of the Jomolhari region, suggest that brittle faulting on extensional structures might be ongoing [*Meyer et al.*, 2006; *Wiesmayr et al.*, 2002].

Direct constraints on the timing of E-W extension across the YCS are more limited. Previous workers [e.g., *Edwards and Harrison*, 1997; *Wu et al.*, 1998] have suggested that the YCS is entirely younger than the STFS. For example, in the map published by *Wu et al.* [1998], the YCS cuts the STFS and is responsible for an apparent left-lateral separation of the STFS fault trace east and west of the YCS. If this interpretation is correct, constraints on the minimum age of activity of the STFS in this area would require that the southern YCS developed after around 11 Ma. This is consistent with the age of shear zones in the northern extension of the YCS (the Yadong Gulu rift; Figure 1), which suggest that rifting initiated after circa 11.5 Ma [*Ratschbacher et al.*, 2011] and possibly as late as circa 8 Ma [*Harrison et al.*, 1995a]. However, mapping by *Cooper et al.* [2012] cast doubt on the extent to which there is substantial sinistral offset of the STFS across the YCS; in fact, no lateral offset is required based on their mapping. This is consistent with *Wu et al.* [1998], who interpreted the apparent offset to result from differential vertical displacement of the STFS above a lateral ramp in the Main Himalayan Thrust.

Our approach to constraining the relative timing of slip on YCS and STFS structures in this region focused on the clear interaction between the Lingshi fault and the basal STFS detachment in NW Bhutan. Specifically, our objective was to use U-Pb geochronology to date samples from the Paro Chu valley (Figure 2) that constrain cross-cutting relationships between the Lingshi fault and strands of the STFS.

3.1. Leucogranite Samples

In the Jomolhari area, leucogranites in the STFS footwall do not extend into the hanging wall above, implying that they have been truncated by the detachment and therefore that the STFS was active after emplacement. Our U-Pb work on leucogranites was thus motivated by the desire to establish a maximum age for this brittle STFS deformation. In addition, as noted by *Kellett et al.* [2010], ductile fabrics associated with the earliest stages of STFS deformation are commonly found in the leucogranites of Bhutan at high structural levels, and thus, the magmatic ages of these granites also help to constrain the early slip history of the detachment system.

We collected four leucogranite samples for U-Pb zircon geochronology: two samples from the Chung La pluton, one from a deformed dike that crosscuts and postdates host calc-silicate rocks, and one from a boudin in the Lingshi fault zone (Figures 2 and 3). Microstructural examination of each sample reveals
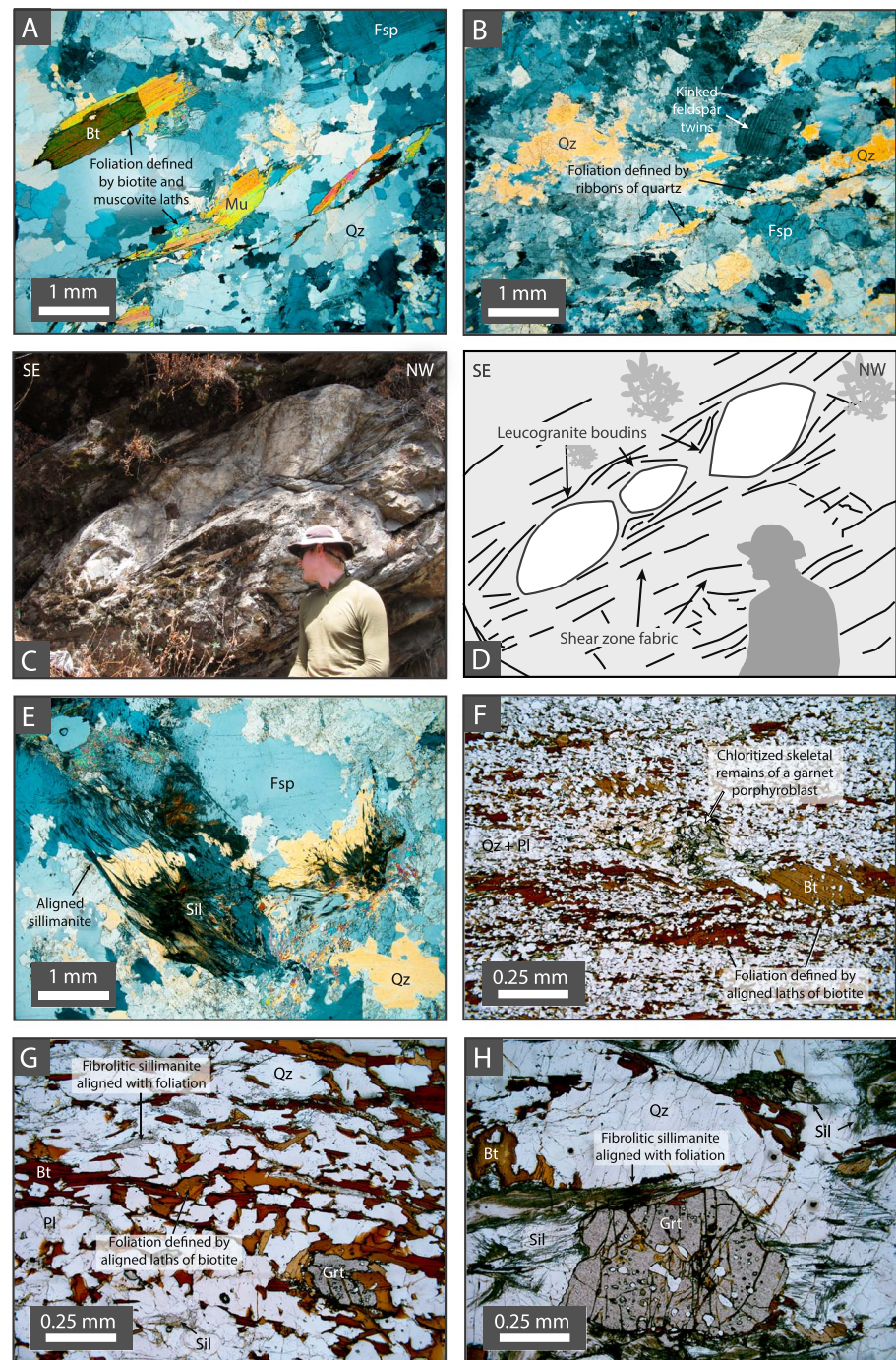
Figure 3. Microscale and macroscale observations of samples used in this study. (a and b) Thin section photomicrographs of leucogranite samples under cross-polarized light. Figure 3a: Chung La granite sample FB108; Figure 3b: Deformed dike sample FB117. (c) Field photograph and (d) line drawing of leucogranite boudins in the Lingshi fault zone from which FB116 was collected. (e) Photomicrograph of sample FB116 under cross-polarized light. (f–h) Thin section photomicrographs of metamorphic samples under plane-polarized light. Figure 3f: FB111; Figure 3g: BT2608; Figure 3h: BT4108.

varying levels of deformation. Chung La pluton samples FB108 and FB109 exhibit a relatively undeformed igneous texture with a weak foliation dipping ~25° to the SSE defined by laths of muscovite and occasionally biotite, while large feldspar, muscovite, quartz, and tourmaline crystals show little to no internal deformation (Figure 3a). Sample FB117, collected from a deformed footwall dike, is a tourmaline-bearing, mica-poor granite that exhibits undulose extinction and recrystallization of quartz, fracturing of

feldspar, and deformation of feldspar twins (Figure 3b). All three samples contain minor amounts of fibrolitic sillimanite, sometimes aligned with the foliation, but often present as small sillimanite sprays with no preferred orientation.

Sample FB116, collected from a ductilely deformed boudin in the Lingshi fault zone (Figures 3c and 3d), is the most strongly deformed. Much of the original igneous texture and mineralogy has been replaced by fibrous sprays of sillimanite, which dominate the mineralogy and indicate a high-temperature, postemplacement metamorphic overprint (Figure 3e). Most of the sillimanite is not aligned, although in places a preferred orientation is observed. However, because the sample was not orientated during sampling, it is not possible to determine precisely what this alignment is related to. *Kellett et al.* [2009] described sillimanite in comparable Bhutan leucogranites as retrograde and suggested that it grew in a subsolidus environment at temperatures above 550°C. This implies that postpeak, but still high-grade metamorphism was ongoing during movement on the Lingshi fault.

3.1.1. U-Pb Zircon Analyses

U-Pb zircon analyses were performed at the Natural Environment Research Council Isotope Geosciences Laboratory (NIGL) in Keyworth, UK. Individual zircons separated from leucogranite samples FB108, FB109, FB116, and FB117 were mounted in epoxy resin and outer grain surfaces analyzed to a depth of ~1–2 μm prior to polishing (Figure 4). U-Pb measurements were made on a Nu Instruments "*Nu Plasma*" high-resolution multicollector, inductively coupled plasma mass spectrometer (MC-ICP-MS) connected to a New Wave Research *UP193ss* laser ablation system. Helium was used as a carrier gas and mixed with argon via a y-piece prior to the plasma torch. Analyses were conducted with simultaneous aspiration of a TI-U solution to monitor mass bias and instrument drift. Normalization for ^{207}Pb-^{206}Pb and ^{238}U-^{206}Pb ratios used a standard-sample bracketing technique with primary reference material Plešovice (337.13 ± 0.37 Ma, ID-TIMS) [*Sláma et al.*, 2008] and secondary reference material 91500 (1063.6 ± 1.4 Ma, ID-TIMS) [*Schoene et al.*, 2006]. The uncertainty on individual ratios is typically 2–3% (2σ).

The epoxy mounts were then polished down to reveal grain interiors, which were imaged in cathodoluminescence (CL) prior to analysis (Figure 4). U-Pb analyses of the polished grains were normalized to GJ-1 (599.8 ± 1.8 Ma, ID-TIMS) [*Jackson et al.*, 2004] as the primary reference material and Plešovice as the secondary. The full analytical methodology follows *Palin et al.* [2013] and is outlined in Table S1 in the supporting information. Data reduction was undertaken using in-house spreadsheets at NIGL, and data were plotted using Isoplot version 3.7 [*Ludwig*, 2003]. Results are provided in Table 1 and supporting information Table S2. All dates are quoted at the 2σ confidence level unless stated otherwise.

3.1.2. Results and Interpretation

Due to the small grain sizes of the analyzed zircons and relative youth of the samples, Pb signals were small, creating relatively large uncertainties on the U-Pb dates. Representative images of analyzed zircons for each sample are given in Figure 4 and concordia plots in Figure 5. Spot analyses of the unpolished outer surfaces of zircons from Chung La pluton samples FB108 and FB109 give a weighted mean, common-Pb corrected ^{238}U/^{206}Pb crystallization date of 21.06 ± 0.27 Ma. Analyses of polished grain interiors reveal inherited low-U Paleozoic cores that appear bright in CL, and dark, high-U igneous rims with a weighted mean crystallization date of 21.70 ± 0.37 Ma, comparable with the outer surface analyses. Results are similar for sample FB117, with grain exteriors giving a weighted mean date of 20.45 ± 0.80 Ma, within error of the Chung La pluton. Zircon interiors show a similar zonation pattern, with Proterozoic to Paleozoic cores surrounded by Miocene rims providing a weighted mean date of 21.80 ± 1.50 Ma.

Together, external rim analyses from the three footwall samples constrain the timing of granite emplacement to circa 21 Ma. This is, broadly consistent with other early Miocene leucogranite ages reported in Bhutan [e.g., *Kellett et al.*, 2009, 2013] as well as numerous other locations across the Himalaya (e.g., Manaslu, Nepal: *Harrison et al.* [1995b]; Annapurna, Nepal: *Hodges et al.* [1996]; Kung Co, Tibet: *Lee et al.* [2011] and *Maheo et al.* [2007]; Sikkim, India: *Rubatto et al.* [2013]; Shivling, India: *Searle et al.* [1999]). However, it is considerably older than the nearby circa 12.5 Ma Khula Kangri granite in southern Tibet [*Edwards and Harrison*, 1997] and the youngest zircon rim age for a deformed STFS footwall dike in the Masang Kang area [*Kellett et al.*, 2009].

Rim dates from multiple zircons in sample FB116, the deformed leucogranite collected within the Lingshi fault zone, suggest a more complicated crystallization history (Figures 5g and 5h). Twenty-one analyses of
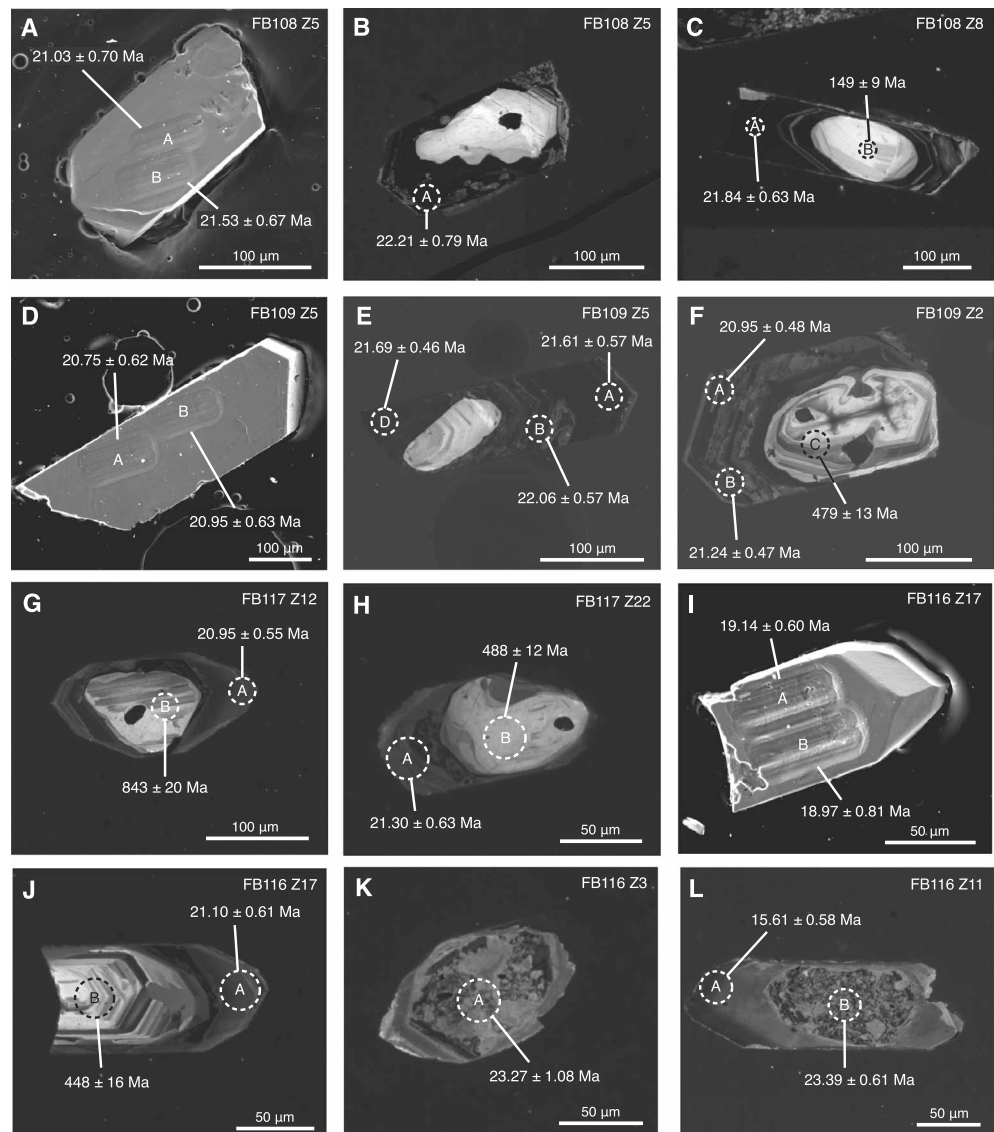
Figure 4. Representative analyzed zircons from the four leucogranites. (a–f) Samples FB108 and FB109: (Figure 4a) Backscattered electron (BSE) image of ~1–2 μm deep ablation pits on the outer surface of FB108 zircon 5, avoiding older, inherited zones and cores. (Figure 4b) Cathodoluminescence (CL) image of the same grain polished to reveal its interior with a low-U inherited core (bright in CL) and a darker high-U igneous rim. (Figure 4c) CL image of FB108 zircon 8 illustrating the inherited early Cretaceous core relative to the early Miocene rim. (Figures 4d and 4e) BSE and CL images of FB109 zircon 5. (Figure 4f) CL image of FB109 zircon 2 revealing a low-U inherited Paleozoic core and an early Miocene rim. (Figures 4g and 4h) Sample FB117: CL images of polished grains reveal complicated interiors with low-U inherited Precambrian-Paleozoic cores (bright in CL) and darker high-U early Miocene igneous rims. (i–l) Sample FB116: (Figure 4i) BSE image of ~1–2 μm deep ablation pits on the external surface of a zircon, avoiding older, inherited zones and cores. (Figure 4j) CL image of the same grain polished to reveal a complicated interior with a low-U inherited Cambrian age core (bright in CL) and a darker high-U early Miocene igneous rim, similar to zircons in the other leucogranite samples. (Figures 4k and 4l) CL images showing examples of polished grain interiors observed in all other zircons from the sample. These grains reveal a very different internal structure with sponge-like textured early Miocene cores surrounded by dark middle Miocene igneous rims.

unpolished grain surfaces give a significant spread of dates along concordia from 23.00 ± 0.74 Ma to 13.84 ± 0.48 Ma. Five analyses of polished interiors give a slightly more coherent picture, with four analyses yielding a weighted mean date of 22.30 ± 1.80 Ma and one analysis giving a date of 15.61 ± 0.58 Ma. CL images of these polished interiors reveal a distinct textural difference between the two age groupings. Zircons with the older rims contain bright, inherited, Paleozoic cores. Zircons with younger rims have Miocene age cores with a mottled appearance, surrounded by dark, younger rims (Figures 4k and 4l).

Table 1. U-Pb Zircon Analyses

Sample	Settings	Pb (ppm)	U (ppm)	238U/206Pb	1σ (%)	207Pb/206Pb	1σ (%)	207Pb/235U	1σ (%)	206Pb/238U	1σ (%)	Rho	f206	238U/206Pb Age (Ma)	2σ (Ma)
						FB108 Zircon Grain Surfaces									
1A	20 s, 5 Hz	11	995	291.06	1.61	0.0465	1.07	0.0220	1.93	0.0034	1.61	0.83	0.000	22.11	0.71
1B	20 s, 5 Hz	23	2035	297.39	1.71	0.0486	0.70	0.0225	1.85	0.0034	1.71	0.93	0.003	21.58	0.74
1C	20 s, 5 Hz	25	2287	298.05	1.56	0.0512	1.24	0.0237	1.99	0.0034	1.56	0.78	0.006	21.46	0.67
2A	20 s, 5 Hz	22	2114	318.56	2.33	0.0520	1.01	0.0225	2.54	0.0031	2.33	0.92	0.007	20.06	0.94
2B	20 s, 5 Hz	9	855	303.96	1.55	0.0460	1.25	0.0209	1.99	0.0033	1.55	0.78	−0.001	21.18	0.66
3A	20 s, 5 Hz	14	1347	326.53	2.97	0.0563	3.09	0.0238	4.29	0.0031	2.97	0.69	0.013	19.47	1.16
3B	20 s, 5 Hz	23	1965	279.60	2.01	0.0974	4.94	0.0480	5.33	0.0036	2.01	0.38	0.064	21.53	0.87
5A	20 s, 5 Hz	11	1004	305.69	1.67	0.0474	1.27	0.0214	2.09	0.0033	1.67	0.80	0.001	21.03	0.70
5B	20 s, 5 Hz	9	790	299.14	1.56	0.0459	1.44	0.0211	2.12	0.0033	1.56	0.74	−0.001	21.53	0.67
8A	20 s, 5 Hz	11	987	296.82	1.56	0.0460	1.11	0.0214	1.91	0.0034	1.56	0.81	−0.001	21.69	0.68
8B	20 s, 5 Hz	12	1051	292.41	1.55	0.0458	1.06	0.0216	1.87	0.0034	1.55	0.82	−0.001	22.03	0.68
12A	20 s, 5 Hz	21	1874	296.58	1.51	0.0509	1.28	0.0237	1.98	0.0034	1.51	0.76	0.006	21.58	0.65
12B	20 s, 5 Hz	23	2046	298.65	1.69	0.0497	0.68	0.0229	1.82	0.0033	1.69	0.93	0.004	21.46	0.73
12C	20 s, 5 Hz	14	1277	294.95	1.56	0.0579	2.52	0.0270	2.96	0.0034	1.56	0.53	0.014	21.50	0.67
9A	20 s, 5 Hz	25	2322	298.35	1.53	0.0524	1.02	0.0242	1.84	0.0034	1.53	0.83	0.008	21.41	0.66
						FB108 Zircon Grain Interiors									
5A	20 s, 5 Hz	79	24778	283.38	1.77	0.0638	3.15	0.0311	3.61	0.0035	1.77	0.49	0.022	22.21	0.79
8A	20 s, 5 Hz	90	28904	294.12	1.43	0.0478	0.34	0.0224	1.47	0.0034	1.43	0.97	0.002	21.84	0.63
8B	20 s, 5 Hz	11	473	37.87	2.88	0.1379	0.79	0.5020	2.98	0.0264	2.88	0.96	0.112	149.5	8.7
						FB109 Zircon Grain Surfaces									
2A	20 s, 5 Hz	6	580	291.34	1.47	0.0880	2.47	0.0416	2.87	0.0034	1.47	0.51	0.053	20.93	0.62
2B	20 s, 5 Hz	8	763	303.41	1.60	0.0480	1.70	0.0218	2.33	0.0033	1.60	0.69	0.002	21.17	0.68
3A	20 s, 5 Hz	11	1088	312.28	2.01	0.0537	4.01	0.0237	4.48	0.0032	2.01	0.45	0.009	20.42	0.82
3B	20 s, 5 Hz	9	860	317.06	1.51	0.0891	4.77	0.0387	5.00	0.0032	1.51	0.30	0.054	19.21	0.58
4A	20 s, 5 Hz	10	955	315.12	1.54	0.0493	1.72	0.0216	2.31	0.0032	1.54	0.67	0.004	20.35	0.63
5A	20 s, 5 Hz	15	1382	309.98	1.50	0.0469	0.87	0.0209	1.73	0.0032	1.50	0.86	0.001	20.75	0.62
5B	20 s, 5 Hz	16	1531	306.94	1.51	0.0471	0.80	0.0212	1.71	0.0033	1.51	0.88	0.001	20.95	0.63
6A	20 s, 5 Hz	16	1382	293.73	1.57	0.0586	2.14	0.0275	2.65	0.0034	1.57	0.59	0.015	21.57	0.68
7A	20 s, 5 Hz	12	1131	312.22	1.67	0.0453	1.23	0.0200	2.08	0.0032	1.67	0.81	−0.001	20.64	0.69
7B	20 s, 5 Hz	17	1602	304.84	1.68	0.0528	1.25	0.0239	2.09	0.0033	1.68	0.80	0.008	20.94	0.71
7C	20 s, 5 Hz	6	519	293.64	1.71	0.0477	2.03	0.0224	2.66	0.0034	1.71	0.64	0.002	21.88	0.75
9A	20 s, 5 Hz	12	1173	311.63	1.90	0.0462	1.08	0.0204	2.19	0.0032	1.90	0.87	0.000	20.66	0.79
9B	20 s, 5 Hz	14	1298	302.89	1.76	0.0524	1.60	0.0239	2.37	0.0033	1.76	0.74	0.008	21.09	0.74
15A	20 s, 5 Hz	11	1102	322.46	1.91	0.0461	1.21	0.0197	2.26	0.0031	1.91	0.84	0.000	19.97	0.76
						FB109 Zircon Grain Interiors									
2A	20 s, 5 Hz	42	13338	305.52	1.15	0.0509	0.62	0.0230	1.30	0.0033	1.15	0.88	0.006	20.95	0.48
2B	20 s, 5 Hz	38	12367	302.46	1.11	0.0479	0.71	0.0218	1.31	0.0033	1.11	0.84	0.002	21.24	0.47
2C	20 s, 5 Hz	42	580	12.84	1.34	0.0645	0.52	0.6925	1.43	0.0779	1.34	0.93	0.010	479	13
5A	20 s, 5 Hz	79	24829	292.72	1.31	0.0599	3.52	0.0282	3.76	0.0034	1.31	0.35	0.017	21.61	0.57
5B	20 s, 5 Hz	98	28716	274.93	1.28	0.0919	5.55	0.0461	5.70	0.0036	1.28	0.22	0.057	22.06	0.57
5D	20 s, 5 Hz	61	19515	296.17	1.05	0.0478	0.49	0.0223	1.16	0.0034	1.05	0.91	0.002	21.69	0.46
10A	20 s, 5 Hz	111	33565	280.12	1.26	0.0882	2.95	0.0434	3.21	0.0036	1.26	0.39	0.053	21.76	0.55
10B	20 s, 5 Hz	83	25349	278.51	1.13	0.0829	4.11	0.0410	4.26	0.0036	1.13	0.26	0.046	22.04	0.50
18A	20 s, 5 Hz	45	13567	273.37	1.20	0.0683	6.31	0.0344	6.42	0.0037	1.20	0.19	0.028	22.89	0.55
18B	20 s, 5 Hz	33	10841	303.46	1.13	0.0472	0.85	0.0214	1.42	0.0033	1.13	0.80	0.001	21.19	0.48
25B	20 s, 5 Hz	134	806	5.42	1.09	0.0771	0.17	1.9601	1.11	0.1845	1.09	0.99	0.001	1090	26
						FB116 Zircon Grain Surfaces									
2A	20 s, 5 Hz	6	517	300.04	1.67	0.0513	3.99	0.0236	4.32	0.0033	1.67	0.39	0.006	21.32	0.71

Table 1. (continued)

Sample	Settings	Pb (ppm)	U (ppm)	$^{238}U/^{206}Pb$	1σ (%)	$^{207}Pb/^{206}Pb$	1σ (%)	$^{207}Pb/^{235}U$	1σ (%)	$^{206}Pb/^{238}U$	1σ (%)	Rho	f206	$^{238}U/^{206}Pb$ Age (Ma)	2σ (Ma)
2B	20 s, 5 Hz	5	386	292.92	1.66	0.0502	2.43	0.0236	2.95	0.0034	1.66	0.56	0.005	21.87	0.73
3A	20 s, 5 Hz	2	275	426.92	1.54	0.0516	3.79	0.0167	4.09	0.0023	1.54	0.38	0.007	14.98	0.46
4A	20 s, 5 Hz	2	256	399.74	1.67	0.0503	3.95	0.0173	4.28	0.0025	1.67	0.39	0.005	16.03	0.54
4B	20 s, 5 Hz	3	294	339.96	1.87	0.0497	3.25	0.0202	3.75	0.0029	1.87	0.50	0.004	18.86	0.70
2A	20 s, 10 Hz	21	1859	311.80	1.85	0.0790	2.81	0.0349	3.36	0.0032	1.85	0.55	0.041	19.79	0.73
2B	20 s, 10 Hz	18	1372	279.27	1.60	0.0479	0.73	0.0237	1.76	0.0036	1.60	0.91	0.002	23.00	0.74
3A	20 s, 10 Hz	6	626	400.22	1.63	0.0470	1.99	0.0162	2.57	0.0025	1.63	0.63	0.001	16.08	0.53
4A	20 s, 10 Hz	9	771	316.16	2.30	0.0492	1.30	0.0215	2.64	0.0032	2.30	0.87	0.004	20.29	0.93
4B	20 s, 10 Hz	10	812	294.67	1.70	0.0507	1.49	0.0237	2.26	0.0034	1.70	0.75	0.005	21.72	0.74
8A	20 s, 5 Hz	4	379	300.31	1.69	0.0788	0.50	0.0362	1.76	0.0033	1.69	0.96	0.041	20.55	0.70
9A	20 s, 5 Hz	6	544	305.76	1.73	0.0515	2.81	0.0232	3.30	0.0033	1.73	0.52	0.006	20.91	0.72
9B	20 s, 5 Hz	13	1133	291.15	1.78	0.0623	2.81	0.0295	3.33	0.0034	1.78	0.54	0.020	21.66	0.77
11A	20 s, 5 Hz	10	1338	455.44	1.58	0.0469	1.17	0.0142	1.97	0.0022	1.58	0.80	0.001	14.13	0.45
11B	20 s, 10 Hz	9	1126	449.04	1.53	0.0552	0.50	0.0169	1.61	0.0022	1.53	0.95	0.011	14.18	0.43
15A	20 s, 10 Hz	9	1202	463.15	1.73	0.0500	1.94	0.0149	2.60	0.0022	1.73	0.67	0.005	13.84	0.48
17A	20 s, 10 Hz	15	1395	316.80	1.57	0.0923	3.60	0.0402	3.93	0.0032	1.57	0.40	0.058	19.14	0.60
17B	20 s, 10 Hz	27	2701	338.48	2.14	0.0485	0.62	0.0198	2.23	0.0030	2.14	0.96	0.003	18.97	0.81
11C	20 s, 5 Hz	4	573	448.44	1.58	0.0481	2.51	0.0148	2.97	0.0022	1.58	0.53	0.002	14.33	0.45
11D	20 s, 5 Hz	4	592	454.04	1.58	0.0505	2.39	0.0153	2.87	0.0022	1.58	0.55	0.005	14.11	0.45
15A	20 s, 5 Hz	3	438	426.50	1.69	0.0500	2.84	0.0162	3.30	0.0023	1.69	0.51	0.005	15.03	0.51
FB116 Zircon Grain Interiors															
3A	20 s, 10 Hz	16	4804	274.27	2.32	0.0529	1.54	0.0266	2.79	0.0036	2.32	0.83	0.008	23.27	1.08
9A	20 s, 10 Hz	27	9429	290.83	1.71	0.0534	2.00	0.0253	2.63	0.0034	1.71	0.65	0.009	21.93	0.75
11A	20 s, 10 Hz	16	7216	411.16	1.87	0.0487	1.60	0.0163	2.46	0.0024	1.87	0.76	0.003	15.61	0.58
11B	20 s, 10 Hz	27	7892	271.89	1.29	0.0558	1.96	0.0283	2.35	0.0037	1.29	0.55	0.012	23.39	0.61
17A	20 s, 10 Hz	11	3770	303.59	1.45	0.0502	1.95	0.0228	2.43	0.0033	1.45	0.60	0.005	21.10	0.61
17B	20 s, 10 Hz	56	835	13.84	1.71	0.0583	0.42	0.5812	1.76	0.0723	1.71	0.97	0.003	448	16
FB117 Zircon Grain Surfaces															
1A	20 s, 10 Hz	10	861	298.18	2.53	0.0481	1.51	0.0222	2.94	0.0034	2.53	0.86	0.002	21.54	1.09
1B	20 s, 10 Hz	34	2423	236.31	4.72	0.0839	4.30	0.0489	6.39	0.0042	4.72	0.74	0.047	25.93	2.45
3A	20 s, 10 Hz	24	1850	260.64	2.10	0.1705	8.21	0.0902	8.48	0.0038	2.10	0.25	0.157	20.82	0.88
5A	20 s, 10 Hz	7	491	236.47	3.84	0.1660	12.66	0.0968	13.23	0.0042	3.84	0.29	0.151	23.10	1.78
5B	20 s, 10 Hz	8	711	284.80	2.54	0.0481	1.65	0.0233	3.03	0.0035	2.54	0.84	0.002	22.55	1.15
6A	20 s, 10 Hz	6	587	307.29	1.71	0.0444	1.89	0.0199	2.55	0.0033	1.71	0.67	−0.003	21.00	0.72
6B	20 s, 10 Hz	6	471	291.83	2.81	0.0611	8.18	0.0289	8.64	0.0034	2.81	0.32	0.019	21.64	1.22
12A	20 s, 10 Hz	6	528	308.45	4.27	0.0449	2.25	0.0201	4.83	0.0032	4.27	0.88	−0.002	20.91	1.79
11A	20 s, 10 Hz	9	766	267.08	3.28	0.0975	13.35	0.0503	13.75	0.0037	3.28	0.24	0.065	22.54	1.48
11B	20 s, 10 Hz	6	564	290.43	3.51	0.0798	8.69	0.0379	9.38	0.0034	3.51	0.37	0.042	21.22	1.49
10A	20 s, 10 Hz	4	396	322.77	1.47	0.0436	4.01	0.0186	4.27	0.0031	1.47	0.34	−0.004	20.01	0.59
9A	20 s, 10 Hz	10	917	295.23	1.86	0.0659	2.70	0.0308	3.28	0.0034	1.86	0.57	0.025	21.26	0.79
9B	20 s, 10 Hz	8	745	293.68	1.90	0.0688	5.60	0.0323	5.92	0.0034	1.90	0.32	0.028	21.30	0.81
8A	20 s, 10 Hz	3	338	377.29	1.83	0.0704	10.61	0.0257	10.77	0.0027	1.83	0.17	0.030	16.55	0.61
7A	20 s, 10 Hz	7	626	295.70	1.55	0.0615	8.05	0.0287	8.19	0.0034	1.55	0.19	0.019	21.35	0.66
7B	20 s, 10 Hz	7	587	289.73	2.00	0.1198	6.88	0.0570	7.17	0.0035	2.00	0.28	0.093	20.15	0.81
24A	20 s, 10 Hz	1	111	303.73	2.34	0.0549	7.34	0.0249	7.71	0.0033	2.34	0.30	0.011	20.96	0.98
34B	20 s, 10 Hz	2	143	233.93	6.03	0.3186	9.45	0.1878	11.21	0.0043	6.03	0.54	0.344	18.05	2.18
30A	20 s, 10 Hz	4	350	331.88	2.83	0.0536	6.25	0.0223	6.86	0.0030	2.83	0.41	0.009	19.22	1.09
29A	20 s, 10 Hz	3	299	312.82	3.15	0.0506	5.82	0.0223	6.62	0.0032	3.15	0.48	0.005	20.47	1.29
28A	20 s, 10 Hz	8	522	227.68	4.57	0.1776	11.27	0.1076	12.16	0.0044	4.57	0.38	0.166	23.57	2.16

Table 1. (continued)

Sample	Settings	Pb (ppm)	U (ppm)	$^{238}U/^{206}Pb$	1σ (%)	$^{207}Pb/^{206}Pb$	1σ (%)	$^{207}Pb/^{235}U$	1σ (%)	$^{206}Pb/^{238}U$	1σ (%)	Rho	f206	$^{238}U/^{206}Pb$ Age (Ma)	2σ (Ma)
						FB117 Zircon Grain Interiors									
4A	20 s, 10 Hz	20	6059	279.24	1.43	0.0812	7.79	0.0401	7.92	0.0036	1.43	0.18	0.044	22.03	0.63
11A	20 s, 10 Hz	36	12078	300.40	1.53	0.0482	0.76	0.0221	1.71	0.0033	1.53	0.90	0.002	21.38	0.66
11B	20 s, 10 Hz	11	3220	253.91	1.37	0.0879	1.95	0.0477	2.39	0.0039	1.37	0.57	0.052	24.01	0.66
12A	20 s, 10 Hz	11	3747	306.75	1.32	0.0475	2.05	0.0214	2.44	0.0033	1.32	0.54	0.001	20.95	0.55
22A	20 s, 10 Hz	8	2566	299.69	1.47	0.0530	3.49	0.0244	3.78	0.0033	1.47	0.39	0.008	21.30	0.63
12B	20 s, 10 Hz	134	1050	7.14	1.08	0.0693	0.18	1.3378	1.10	0.1401	1.08	0.99	0.003	843	20
22B	20 s, 10 Hz	21	285	12.71	1.18	0.0578	1.01	0.6271	1.55	0.0787	1.18	0.76	0.001	488	12

Similarly prolonged accessory phase growth was documented in NW Bhutan by *Kellett et al.* [2009] and has also been observed in other Himalayan leucogranites (e.g., *Lederer et al.* [2013]: Leo Pargil dome, India; *Viskupic et al.* [2005]: Everest region, Nepal). *Viskupic et al.* [2005] interpreted this age spread to reflect incremental melting and crystallization of the granite in the source region prior to mobilization and migration of melts containing a mixture of accessory minerals of different ages that record the history of anatexis. Following this interpretation, we take the youngest date in sample FB116 of circa 14 Ma to represent the time of leucogranite emplacement and interpret the older dates as inherited earlier phases of melting and crystallization.

3.2. Metasedimentary Samples

Three STFS footwall metasedimentary samples were collected in outcrop along the Paro Chu valley, both within and away from the Lingshi fault zone (Figure 2). Locations correspond closely with previous sampling by *Kellett et al.* [2010] and *Regis et al.* [2014], and our microstructural and mineralogical observations closely agree with both studies.

FB111, located on the eastern downthrown block along the trace of the Lingshi fault, is a medium-grained, garnet-bearing mica schist dominated by quartz, plagioclase, and biotite, with minor muscovite and sillimanite (Figure 3f). The primary foliation, carried by laths of biotite, lies parallel to the fault zone, dipping 35° to the SSE. Skeletal garnet porphyroblasts, heavily altered to chlorite, suggest retrogression, possibly due to prolonged tectonic activity and fluid flow in the vicinity of the fault zone. Fibrolitic sillimanite aligned with the foliation implies that the Lingshi fault experienced ductile deformation during high-temperature metamorphism.

BT2608, collected ~5 km SE of the Lingshi fault trace, is a garnet-bearing pelitic gneiss defined by alternating bands dominated either by biotite or by quartz and plagioclase along with minor muscovite and K-feldspar (Figure 3g). Fibrolitic sillimanite needles are also prevalent and lie parallel to the main, gently north dipping, foliation. Garnet porphyroblasts have largely broken down to biotite and, in places, sillimanite, which we interpret as the result of interaction with anatectic melt and associated fluids (garnet + K-feldspar + melt + $H_2O \rightarrow$ biotite + sillimanite + quartz) [e.g., *Searle et al.*, 1999]. The garnets preserve inclusion trails of quartz and biotite at a high angle to the main foliation that indicate the presence of an earlier deformation fabric.

BT4108, collected approximately 15 km SE of the Lingshi fault trace, also has a north dipping foliation (Figure 2a). It is a coarse-grained quartz-rich, garnet-bearing pelitic gneiss with minor biotite and K-feldspar, and no visible muscovite or plagioclase. Large millimeter-scale garnets are heavily fractured and often rimmed by retrogressive biotite and sillimanite (Figure 3h). Quartz and biotite inclusion trails preserve an earlier deformation fabric similar to BT2608. Sprays of sillimanite are prevalent across the sample, most aligned with the primary foliation, and others with no preferred orientation.

3.2.1. U-Pb Monazite and Xenotime Analyses

Accessory phases in samples FB111, BT2608, and BT4108 were located in polished thin sections using a JEOL JXA-8200 electron microprobe at the University of California, Los Angeles, and analyzed at NIGL in situ
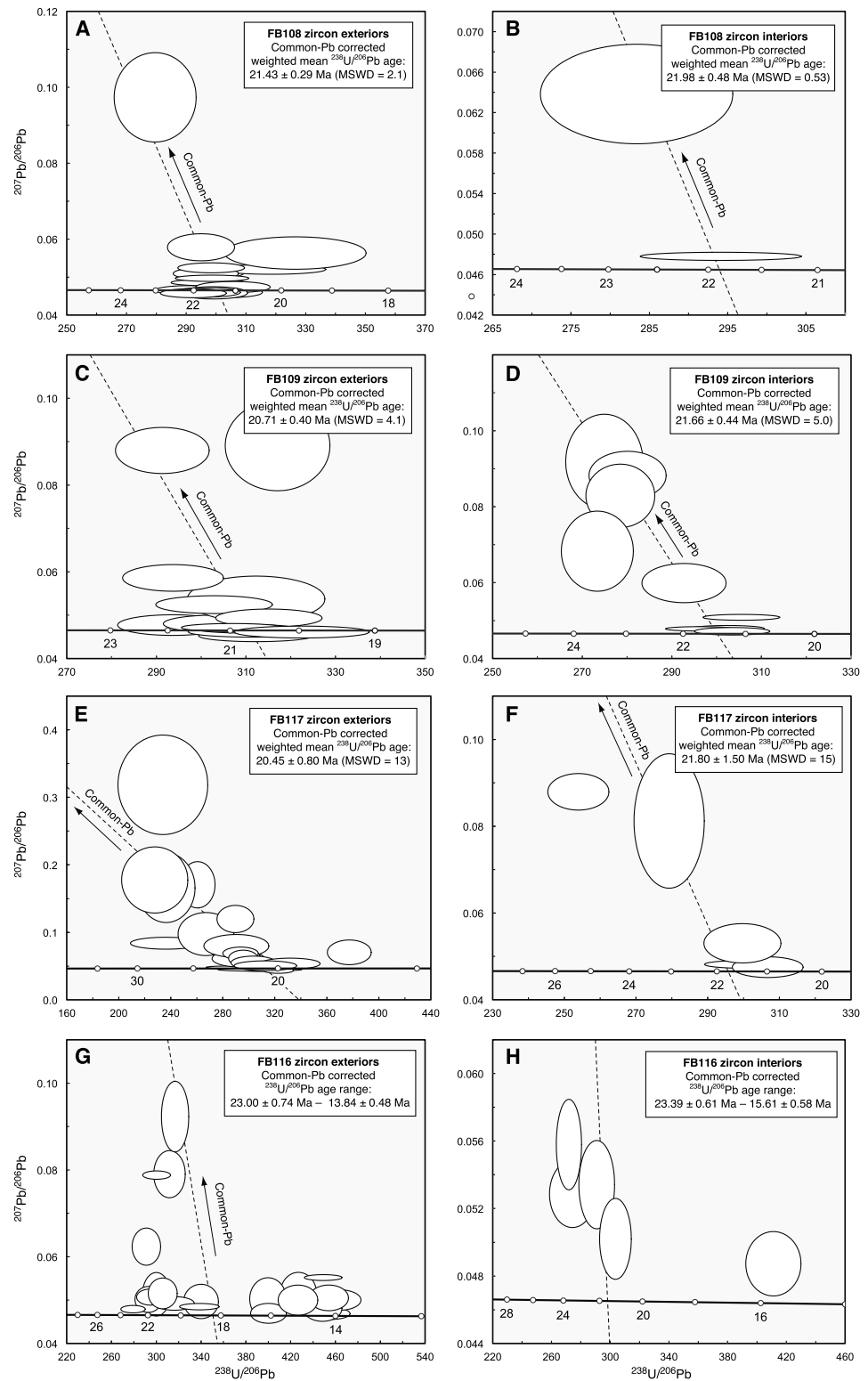
Figure 5. Tera-Wasserburg plots of zircon analyses. All ellipses are shown at the 2σ confidence level. Dashed lines indicate regressions from a common Pb ratio of 0.84 ± 0.02. (a to f) Samples FB108, FB109, and FB117. Analyses of unpolished grain exteriors and polished interiors, excluding older inherited cores, give weighted mean U-Pb ages of circa 21 Ma. (g) External surface analyses of zircons from sample FB116 instead show a spread of ages from 23.00 ± 0.74 Ma to 13.84 ± 0.48 Ma. (h) FB116 grain interior analyses, not including inherited cores, show a similar age spread from 23.39 ± 0.61 Ma to 15.61 ± 0.58 Ma.
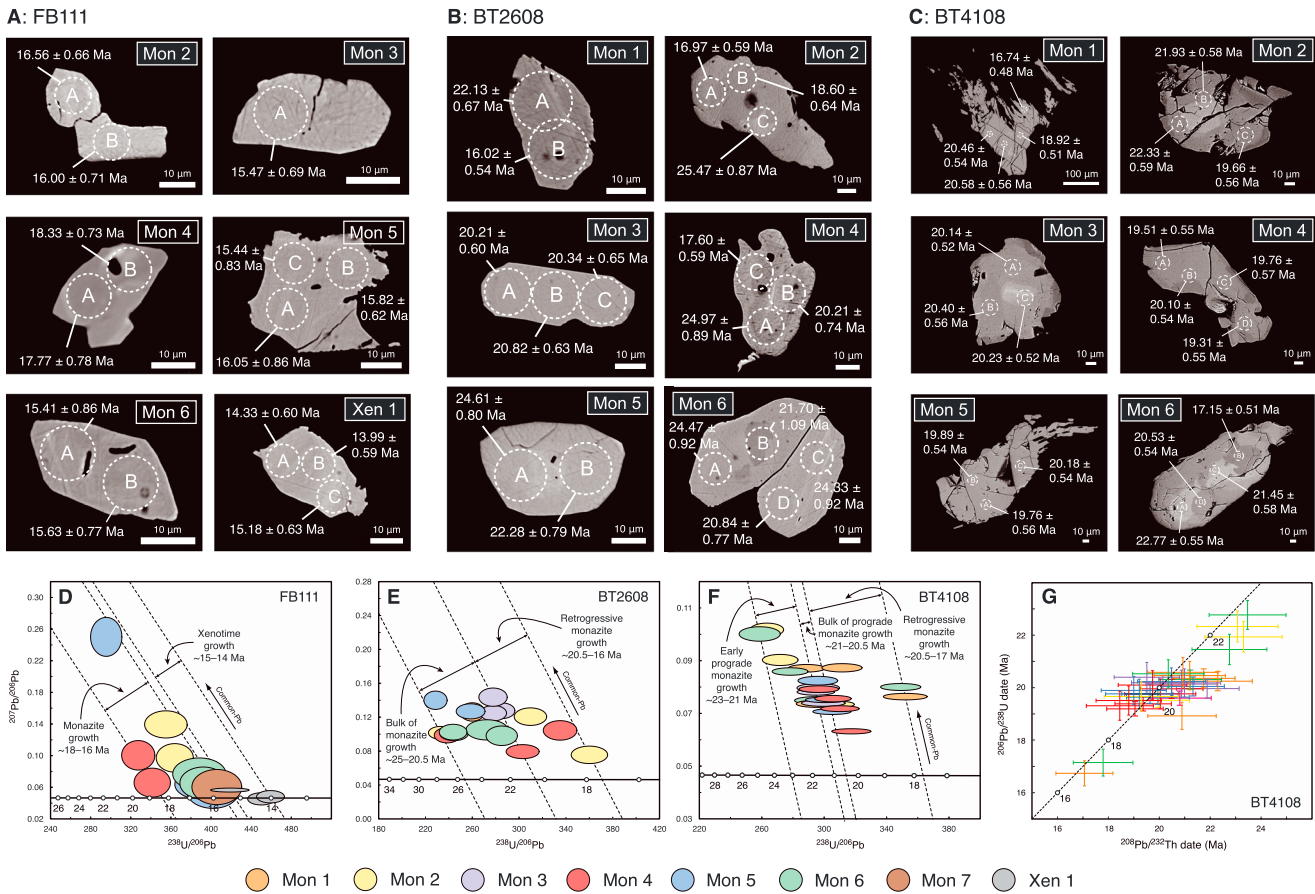
Figure 6. (a–c) BSE images of analyzed monazite and xenotime grains from samples FB111, BT2608, and BT4108. Individual analysis spots are shown with their corresponding U-Pb ages (2σ confidence level). In FB111 and BT2608, all grains were situated in the matrix within grains of quartz, plagioclase, or biotite. In BT4108, all grains were in the matrix except monazite 4, which was included in the garnet porphyroblast shown in Figure 3h. (d–f) Tera-Wasserburg plots of monazite and xenotime U-Pb analyses. Ellipses are shown at the 2σ confidence level. Dashed lines indicate regressions from an assumed common Pb ratio of 0.84 ± 0.02. (g) U-Pb versus Th-Pb monazite concordia plot for sample BT4108. Error bars represent 2σ uncertainties.

to preserve their microtextural context (analyses of individual grains are given in Figure 6 and grains shown in microstructural context are provided in supporting information Figures S1–S3).

Metamorphic monazite and xenotime grains in sample FB111 are exclusively found in the matrix within quartz, plagioclase, and biotite. They are small, typically 30–40 μm in diameter, subhedral, and exhibit no obvious internal zonation in BSE images (Figure 6a). Monazites in sample BT2608 are slightly larger, ranging in size from approximately 30–80 μm in diameter (Figure 6b). Some of the larger grains exhibit internal zoning in BSE that corresponds to variations in the concentration of U, Th, and Y (e.g., monazite 6; U, Th, and Y maps provided in supporting information Figure S2). Sample BT4108 contains much larger monazites, some of which are highly irregular in shape, and all of which are zoned in BSE (Figure 6c). All grains are located in the matrix apart from monazite 4, which is included in the core of the garnet porphyroblast shown in Figure 3h (see also supporting information Figure S3).

U-Pb measurements for samples FB111 and BT2608 were made on the Nu Instruments *Plasma* MC-ICP-MS (Table 2), whereas sample BT4108 was analyzed on a Nu Instruments *Attom* high-resolution single-collector ICP-MS (SC-ICP-MS) (Table 3). U-Pb (and Th-Pb on the Attom) monazite data were normalized to primary reference materials Moacyr (515.6 ± 1.4 Ma, ID-TIMS) or Stern (512.1 ± 1.9 Ma, ID-TIMS), while secondary reference material Manangotry (559 ± 1 Ma, ID-TIMS) was analyzed to monitor accuracy and precision. ID-TIMS dates are from *Palin et al.* [2013]. U-Pb xenotime data were normalized to an in-house primary xenotime reference material, FC-1 (55.6 ± 1.3 Ma, in-house ID-TIMS). Dates of inferred monazite and xenotime growth are derived from U-Pb measurements only since correlative Th-Pb results were only obtained for sample BT4108 on the Nu Attom (Figure 6). Lower intercepts in Tera-Wasserburg concordia

Table 2. U-Pb Monazite and Xenotime Analyses

Sample	Settings	Pb (ppm)	U (ppm)	^{238}U/^{206}Pb	1σ (%)	^{207}Pb/^{206}Pb	1σ (%)	^{207}Pb/^{235}U	1σ (%)	^{206}Pb/^{238}U	1σ (%)	Rho	f206	f208	^{238}U/^{206}Pb Age (Ma)	2σ (Ma)
						FB111 Monazite										
2A	20 s, 5 Hz	14	180	363.85	2.08	0.09708	7.60	0.03679	7.88	0.00275	2.08	0.264	0.06	n/a	16.56	0.66
2B	20 s, 5 Hz	5	193	354.99	2.44	0.13943	5.03	0.05416	5.59	0.00282	2.44	0.436	0.12	n/a	16.00	0.71
3A	20 s, 5 Hz	2	47	197.76	2.38	0.46123	3.65	0.32158	4.35	0.00506	2.38	0.547	0.52	n/a	15.47	0.69
4A	20 s, 5 Hz	37	156	341.38	2.17	0.06583	11.37	0.02659	11.58	0.00293	2.17	0.187	0.02	0.01	17.77	0.78
4B	20 s, 5 Hz	11	155	327.44	2.06	0.10039	7.58	0.04227	7.85	0.00305	2.06	0.263	0.07	0.08	18.33	0.73
5A	20 s, 5 Hz	13	174	389.88	2.72	0.06371	12.24	0.02253	12.53	0.00256	2.72	0.217	0.02	0.02	16.05	0.86
5B	20 s, 5 Hz	18	116	295.55	2.16	0.25012	4.01	0.11668	4.56	0.00338	2.16	0.473	0.26	0.20	15.82	0.62
5C	20 s, 5 Hz	23	155	401.80	2.65	0.05503	16.09	0.01889	16.30	0.00249	2.65	0.162	0.01	0.01	15.44	0.83
6A	20 s, 5 Hz	29	159	388.33	2.79	0.07674	10.83	0.02725	11.18	0.00258	2.79	0.250	0.04	0.02	15.41	0.86
6B	20 s, 5 Hz	24	166	392.30	2.43	0.06515	12.79	0.02290	13.02	0.00255	2.43	0.187	0.02	0.02	15.63	0.77
7A	20 s, 5 Hz	12	149	405.80	2.50	0.06024	15.08	0.02047	15.28	0.00246	2.50	0.164	0.02	0.01	15.53	0.77
						FB111 Xenotime										
1A	20 s, 5 Hz	18	522	450.08	1.23	0.04531	6.96	0.01388	7.07	0.00222	1.23	0.17	0.00	n/a	14.33	0.60
1B	20 s, 5 Hz	18	529	459.31	1.24	0.04799	6.60	0.01441	6.72	0.00218	1.24	0.18	0.00	n/a	13.99	0.59
1C	20 s, 5 Hz	68	1947	418.70	1.87	0.05645	1.81	0.01859	2.60	0.00239	1.87	0.72	0.01	n/a	15.18	0.63
2A	20 s, 5 Hz	35	889	391.15	3.53	0.08819	2.32	0.03109	4.22	0.00256	3.53	0.84	0.05	n/a	15.59	1.16
						BT2608 Monazite										
1A	20 s, 5 Hz	41	247	260.05	1.64	0.12619	3.50	0.06691	3.86	0.00385	1.64	0.43	0.10	0.07	22.13	0.67
1B	20 s, 5 Hz	22	276	314.56	1.81	0.22041	4.17	0.09661	4.55	0.00318	1.81	0.40	0.22	0.15	16.02	0.54
2A	20 s, 5 Hz	57	325	360.06	1.76	0.07558	5.55	0.02894	5.83	0.00278	1.76	0.30	0.04	0.02	16.97	0.59
2B	20 s, 5 Hz	52	284	309.67	1.83	0.12071	3.50	0.05375	3.95	0.00323	1.83	0.46	0.09	0.05	18.60	0.64
2C	20 s, 5 Hz	91	319	232.81	1.80	0.10158	3.05	0.06016	3.54	0.00430	1.80	0.51	0.07	0.03	25.47	0.87
3A	20 s, 5 Hz	36	305	285.06	1.62	0.12762	2.99	0.06173	3.40	0.00351	1.62	0.48	0.10	0.08	20.21	0.60
3B	20 s, 5 Hz	35	319	278.03	1.65	0.12481	2.98	0.06189	3.41	0.00360	1.65	0.49	0.10	0.07	20.82	0.63
3C	20 s, 5 Hz	24	292	277.71	1.78	0.14364	3.07	0.07132	3.55	0.00360	1.78	0.50	0.12	0.09	20.34	0.65
4A	20 s, 5 Hz	60	273	238.51	1.88	0.09876	3.75	0.05709	4.19	0.00419	1.88	0.45	0.07	0.05	24.97	0.89
4B	20 s, 5 Hz	51	365	303.01	1.90	0.07940	4.25	0.03613	4.66	0.00330	1.90	0.41	0.04	0.04	20.21	0.74
4C	20 s, 5 Hz	64	316	335.01	1.75	0.10443	4.51	0.04298	4.84	0.00298	1.75	0.36	0.07	0.04	17.60	0.59
5A	20 s, 5 Hz	53	224	228.59	1.77	0.14001	3.16	0.08445	3.62	0.00437	1.77	0.49	0.12	0.06	24.61	0.80
5B	20 s, 5 Hz	47	357	258.57	1.95	0.12694	2.86	0.06769	3.46	0.00387	1.95	0.56	0.10	0.09	22.28	0.79
6A	20 s, 5 Hz	48	321	244.38	2.01	0.10022	3.20	0.05655	3.78	0.00409	2.01	0.53	0.07	0.06	24.47	0.92
6B	20 s, 5 Hz	38	224	272.51	2.68	0.10508	4.65	0.05316	5.37	0.00367	2.68	0.50	0.07	0.06	21.70	1.09
6C	20 s, 5 Hz	61	256	243.62	1.99	0.10242	3.70	0.05797	4.20	0.00410	1.99	0.47	0.07	0.04	24.33	0.92
6D	20 s, 5 Hz	55	231	285.20	1.91	0.09813	4.79	0.04744	5.16	0.00351	1.91	0.37	0.07	0.04	20.84	0.77

Table 3. U-Th-Pb Monazite Analyses[a]

Sample	Pb (ppm)	Th (ppm)	U (ppm)	238U/206Pb	1σ (%)	207Pb/206Pb	1σ (%)	238U/206Pb	1σ (%)	206Pb/238U	1σ (%)	Rho	208Pb/232Th	1σ (%)	f206	f208	232Th/208Pb age (Ma)	2σ (Ma)	238U/206Pb Age (Ma)	2σ (Ma)
BT4108 Monazite																				
1A	3.2	2595	158	288.8	1.66	0.0871	0.67	0.0416	1.79	0.0035	1.66	0.93	0.0010	2.61	0.05	0.02	20.47	1.32	20.58	0.56
1B	3.4	3019	174	295.2	1.81	0.0736	0.76	0.0344	1.97	0.0034	1.81	0.92	0.0011	2.61	0.03	0.01	20.92	1.36	20.46	0.54
1C	2.5	2603	135	311.5	1.69	0.0873	0.74	0.0386	1.84	0.0032	1.69	0.92	0.0010	2.62	0.05	0.02	20.53	1.30	18.92	0.51
1D	2.0	2820	118	352.0	1.63	0.0763	0.66	0.0299	1.76	0.0028	1.63	0.93	0.0008	2.62	0.04	0.01	16.87	1.09	16.74	0.48
2A	4.3	2524	202	263.3	1.66	0.1017	1.01	0.0533	1.94	0.0038	1.66	0.86	0.0011	2.61	0.07	0.04	22.22	1.48	22.33	0.59
2B	4.0	2464	186	271.8	1.72	0.0903	0.95	0.0458	1.96	0.0037	1.72	0.87	0.0012	2.62	0.06	0.03	22.67	1.44	21.93	0.58
2C	2.5	2293	136	307.2	1.62	0.0734	0.70	0.0330	1.77	0.0033	1.62	0.92	0.0010	2.59	0.03	0.01	19.02	1.41	19.66	0.56
3A	2.7	2493	141	299.5	1.91	0.0739	0.67	0.0340	2.02	0.0033	1.91	0.94	0.0010	2.61	0.03	0.01	20.60	1.36	20.14	0.52
3B	2.6	2207	131	294.6	1.66	0.0781	0.64	0.0366	1.77	0.0034	1.66	0.93	0.0010	2.61	0.04	0.02	19.17	1.24	20.40	0.56
3C	2.8	2510	146	296.2	1.88	0.0797	0.86	0.0371	2.07	0.0034	1.88	0.91	0.0009	2.62	0.04	0.02	20.13	1.29	20.23	0.52
4A	2.6	2379	140	310.1	1.63	0.0718	0.63	0.0319	1.74	0.0032	1.63	0.93	0.0010	2.61	0.03	0.01	18.54	1.25	19.51	0.55
4B	2.5	2549	128	296.6	1.74	0.0792	0.65	0.0368	1.86	0.0034	1.74	0.94	0.0010	2.61	0.04	0.01	19.45	1.31	20.10	0.54
4C	2.9	2363	153	305.7	1.57	0.0756	0.66	0.0341	1.70	0.0033	1.57	0.92	0.0010	2.60	0.04	0.02	19.71	1.35	19.76	0.57
4D	2.7	2337	146	317.4	1.62	0.0632	0.63	0.0275	1.74	0.0032	1.62	0.93	0.0009	2.60	0.02	0.01	18.28	1.29	19.31	0.55
5A	2.1	2238	113	305.0	1.64	0.0707	0.63	0.0320	1.76	0.0033	1.64	0.93	0.0010	2.61	0.03	0.01	19.01	1.30	19.76	0.56
5B	2.2	2406	118	300.9	1.75	0.0751	0.56	0.0344	1.84	0.0033	1.75	0.95	0.0009	2.61	0.04	0.01	18.76	1.25	19.89	0.54
5C	2.7	2375	140	296.0	1.76	0.0824	0.82	0.0384	1.94	0.0034	1.76	0.91	0.0010	2.61	0.05	0.02	20.62	1.37	20.18	0.54
6A	5.4	3134	239	258.7	2.08	0.1001	1.12	0.0534	2.36	0.0039	2.08	0.88	0.0012	2.62	0.07	0.04	22.63	1.40	22.77	0.55
6B	2.9	2673	174	349.1	1.51	0.0800	0.67	0.0316	1.65	0.0029	1.51	0.91	0.0009	2.61	0.04	0.02	17.47	1.13	17.15	0.51
6C	3.5	2616	166	278.1	1.69	0.0859	0.68	0.0426	1.82	0.0036	1.69	0.93	0.0011	2.62	0.05	0.02	22.30	1.41	21.45	0.58
6D	3.1	2516	155	294.4	1.85	0.0749	0.79	0.0351	2.01	0.0034	1.85	0.92	0.0010	2.61	0.04	0.02	20.04	1.36	20.53	0.54

[a]Laser power = 5 Hz; laser dwell time = 20 s.

plots are used for display purposes, but reported dates of individual spot analyses refer to individually common lead-corrected $^{206}Pb/^{238}U$ dates. The common lead correction uses the "^{207}Pb method" [e.g., *Chew et al.*, 2011] and an assumed common lead composition equivalent to a *Stacey and Kramers* [1975] model. Because the analyses are only slightly discordant, the composition of the common lead model used yields only minor variation in the final date. The U-Pb dates are also corrected for excess ^{206}Pb using a correction that assumes a whole rock Th/U ratio of 3. Again, this correction is small (<1 Ma). In Figure 6g, common lead-corrected $^{208}Pb/^{232}Th$ dates calculated for sample BT4108 (based on the ^{207}Pb method and the measured $^{208}Pb/^{206}Pb$ ratio) are plotted against equivalent U-Pb dates. The data fall on the line of concordia, indicating that excess ^{206}Pb is not an issue once corrected for, thus providing confidence in the use of U-Pb rather than Th-Pb dates.

3.2.2. Results and Interpretation

In all three samples, grains large enough for multiple spot analyses show a range in ^{238}U-^{206}Pb dates (Figure 6), probably due to internal U, Th, or Y zonation reflecting a prolonged metamorphic evolution. This is not uncommon and has been observed in numerous studies of metamorphic monazite growth [e.g., *Foster et al.*, 2002; *Gibson et al.*, 2004; *Kelly et al.*, 2012; *Regis et al.*, 2014].

In sample FB111, monazite and xenotime crystals were small and largely unzoned in BSE, and dates within single grains overlap at the 2σ level, making data interpretation relatively straightforward. Individual monazites yield a range of U-Pb dates from 18.33 ± 0.73 Ma to 15.41 ± 0.86 Ma, and xenotimes give a slightly younger range from 15.59 ± 1.16 Ma to 13.99 ± 0.59 Ma (Figure 6d).

In sample BT2608, zonation is visible in some of the BSE images and intracrystalline variability in U-Pb dates is much greater. High-resolution element mapping of monazite 6 allowed us to directly compare this variation with chemical zonation but did not reveal a clear relationship between the two (see supporting information Figure S2). Instead, monazites in the sample exhibit a complex growth, recrystallization and reprecipitation history lasting from 25.47 ± 0.87 Ma to 16.02 ± 0.54 Ma (Figure 6e). This is consistent with results from FB111 as well as previously published work in the area [*Kellett et al.*, 2010; *Regis et al.*, 2014] and GHS rocks farther south, close to the Main Central Thrust [*Tobgay et al.*, 2012].

Sample BT4108 contained much larger grains with stronger internal zonation, yielding apparent age variation within some of the grains, but not all. Four analyses of monazite 4, situated within a garnet porphyroblast, gave a common-Pb corrected weighted mean date of 19.68 ± 0.28 Ma, within error of the other monazites from the same sample. The garnet is heavily cracked, and it is likely that this date reflects chemical reequilibration with the surrounding matrix. Overall, U-Pb dates suggest monazite growth from 22.77 ± 0.55 Ma to 16.74 ± 0.48 Ma, although the majority of growth occurred between circa 21–20.5 Ma (Figure 6f), in close agreement with the timing of major leucogranite emplacement at circa 21 Ma.

Our data suggest that prograde metamorphic monazite growth in the STFS footwall was ongoing between 25 and 20.5 Ma. According to *Regis et al.* [2014], prograde metamorphic monazite growth in this region began as early as 36 Ma. In sample BT2608, the bulk of the monazite growth occurred before circa 20.5 Ma, while in sample BT4108, the majority of growth occurred between 21 and 20.5 Ma. These dates are consistent with the timing of major granite emplacement in the region at 21 Ma and suggest that peak metamorphism and anatexis occurred at this time.

A minimum constraint on prograde metamorphism is more difficult to achieve. However, due to the close temporal relationship between leucogranite zircon crystallization and metamorphic monazite and xenotime growth, we suggest that the youngest monazite and xenotime growth probably resulted from fluid-assisted recrystallization. The fluids could have derived from the nearby magmatic intrusions, devolatization during retrogressive metamorphism, or from pathways generated by crustal fractures [*Gordon et al.*, 2009; *Kellett et al.*, 2010, 2012; *Palin et al.*, 2013]. The younger monazite and xenotime growth in sample FB111, for example, is probably related to its proximity to the more prolonged tectonic and magmatic activity associated with the Lingshi fault zone.

4. Implications for the Timing of Extension in Northwest Bhutan

Our geochronologic data, combined with previous studies in Bhutan [e.g., *Chambers et al.*, 2011; *Corrie et al.*, 2012; *Kellett et al.*, 2010; *Regis et al.*, 2014; *Tobgay et al.*, 2012], suggest that prograde monazite growth in the STFS footwall occurred during amphibolite facies metamorphism from circa 36–20.5 Ma. Following interpretations by previous Himalayan workers [e.g., *Catlos et al.*, 2004; *Groppo et al.*, 2012; *Harrison et al.*, 1999; *Hodges et al.*, 1992; *Kellett et al.*, 2010; *Regis et al.*, 2014], we correlate this prograde metamorphism with synchronous major contractional deformation along the Himalaya. We interpret subsequent monazite and xenotime growth from circa 20.5–14 Ma as retrogressive and a consequence of extensional exhumation related to the South Tibetan fault system. We note that the similar metamorphic histories exhibited by all three metasedimentary samples, whether from the Greater Himalayan sequence or the Chekha Formation (Figure 2b), support our interpretation that both units lie in the footwall of the principal STFS detachment and were unroofed at the same time in the early to middle Miocene.

Early phases of anatexis and leucogranite intrusion at circa 21 Ma are broadly coeval with this transition from prograde to retrograde metamorphism at 20.5–21 Ma, and we follow the long tradition of interpreting slip on the STFS as enhancing the production and upward migration of anatectic melts in the GHS [*Harris and Massey*, 1994]. Detailed studies of migmatites in the Everest region of eastern Nepal [*Groppo et al.*, 2012, 2010], in far-eastern Nepal [*Imayama et al.*, 2012], and in Sikkim, India [*Rubatto et al.*, 2013], suggested that early melting of the GHS at deeper structural levels could be related to prograde metamorphism and that the migration of these melts to higher structural levels beneath the STFS was probably enhanced by decompression related to STFS slip. Following this model for the Jomolhari leucogranites, we infer that generation of the oldest melts at circa 21 Ma was coeval with earliest movement on the STFS.

The STFS-driven decompression process is evidenced in NW Bhutan pelitic samples by the transition from early kyanite-stable conditions to later sillimanite-stable conditions. Monazite inclusions in kyanite from these rocks

demonstrate that the kyanite-to-sillimanite transition occurred sometime after circa 20.5 Ma [*Kellett et al.*, 2010], an observation consistent with our interpretation of decompression by tectonic exhumation of the STFS footwall beginning at circa 21 Ma. The presence of sillimanite in many metapelitic and leucogranite samples collected from this area—including the late, 14 Ma leucogranite involved in ductile Lingshi fault deformation —indicates high-grade metamorphism of the STFS footwall continued until at least 14 Ma.

Based on our geochronologic data alone, it is not possible to place a minimum constraint on STFS slip. However, all three metamorphic samples contain sillimanite lying parallel to the main foliation, suggesting that deformation on the STFS took place at sillimanite facies conditions from at least circa 20.5 to 14 Ma.

The timing of E-W extension on the Yadong cross structure can be constrained by the 14 Ma leucogranite boudin collected in the Lingshi fault zone, which was deformed by, and thus predated, the Lingshi fault. We can infer from this that deformation on the Jomolhari fault system occurred after 14 Ma but still at metamorphic temperatures due to the presence of sillimanite in the granite as well as ductile fabrics and structures preserved in the fault zone.

Although it is not possible to constrain a maximum age for ductile activity on the JFS, the preponderance of available evidence suggests that the Lingshi fault initiated at just about the time that the STFS was experiencing its latest stages of ductile deformation. Synchronous slip on both fault systems must have continued after this time because they each preserve evidence for postmetamorphic, brittle deformation. Significant movement on the STFS was certainly postmetamorphic, first because it corresponds to a metamorphic discontinuity between high-grade GHS rocks in the footwall and low-grade, locally fossiliferous TSS rocks in the hanging wall [e.g., *Cooper et al.*, 2012], and second because the circa 21–14 Ma footwall leucogranites are truncated by the detachment. This is consistent with studies in the Masang Kang, Khula Kangri, and Wagye La regions [*Edwards and Harrison*, 1997; *Kellett et al.*, 2009; *Wu et al.*, 1998], where detachments of the STFS were still active at circa 12.5–11 Ma, and where activity on some structures that may have a similar geodynamic significance to the Miocene STFS may continue today [*Meyer et al.*, 2006; *Wiesmayr et al.*, 2002]. These observations, along with abundant evidence for subsequent brittle, postmetamorphic and postintrusive fabrics and structures of the Jomolhari fault system [e.g., *Wu et al.*, 1998], suggest that both low-angle, ~E-W striking and high-angle, ~NE-SW striking extensional structures in the Jomolhari area had protracted and overlapping deformation histories.

This synchronous history is consistent with mapping by *Cooper et al.* [2012], who showed that the STFS in this area is not significantly offset across the YCS although it is thought to have accommodated some component of strike-slip motion since circa 13 Ma [e.g., *Antolín et al.*, 2012; *Drukpa et al.*, 2006; *Kellett and Grujic*, 2012]. Instead, the data here, together with the previous mapping, suggest a kinematic relationship between the STFS and the YCS in middle Miocene time that, based on documented activity on both structures, continues today. This is contrary to the suggestion by *Edwards and Harrison* [1997] that the YCS cut the STFS and therefore that slip on the STFS ceased prior to development of the YCS.

5. Conclusions

The Jomolhari region of NW Bhutan records evidence of synchronous N-S and E-W extension at the Tibet-to-Himalaya transition in middle Miocene time. Geochronological data combined with microstructural and field observation of the South Tibetan fault system footwall demonstrate that (1) high-grade metamorphism and deformation related to South Tibetan fault system displacement continued until at least 14 Ma; (2) E-W extension on the Jomolhari fault system initiated during this high-grade metamorphism, certainly by 14 Ma; (3) brittle, postmetamorphic and postintrusive fabrics and structures in both fault systems imply that N-S and E-W extensional structures in the Jomolhari area had protracted and overlapping deformation histories; and (4) slip on the South Tibetan fault system did not cease prior to initiation of the Yadong cross structure.

References

Andronicos, C. L., A. A. Velasco, and J. M. Hurtado (2007), Large-scale deformation in the India-Asia collision constrained by earthquakes and topography, *Terra Nova*, *19*, 105–119, doi:10.1111/j.1365-3121.2006.00714.x.
Antolín, B., E. Schill, D. Grujic, S. Baule, X. Quidelleur, E. Appel, and M. Waldhör (2012), E-W extension and block rotation of the southeastern Tibet: Unravelling late deformation stages in the eastern Himalayas (NW Bhutan) by means of pyrrhotite remanences, *J. Struct. Geol.*, *42*, 19–33, doi:10.1016/j.jsg.2012.07.003.

Armijo, R., P. Tapponnier, J. L. Mercier, and H. Tong-Lin (1986), Quaternary extension in southern Tibet: Field observations and tectonic implications, *J. Geophys. Res.*, *91*(B14), 13,803–813,872, doi:10.1029/JB091iB14p13803.

Beaumont, C., R. A. Jamieson, M. H. Nguyen, and B. Lee (2001), Himalayan tectonics explained by extrusion of a low-viscosity crustal channel coupled to focused surface denudation, *Nature*, *414*, 738–742.

Bhargava, O. N. (1995), *The Bhutan Himalaya: A Geological Account*, Geol. Soc. India Spec. Publ., 245 pp., Geol. Soc. of India, Calcutta.

Blisniuk, P. M., B. R. Hacker, J. Glodny, L. Ratschbacher, S. Bi, Z. Wu, M. O. McWilliams, and A. Calvert (2001), Normal faulting in central Tibet since at least 13.5 Myr ago, *Nature*, *412*, 628–632.

Burchfiel, B. C., C. Zhiliang, K. V. Hodges, L. Yuping, L. H. Royden, D. Changrong, and X. Jiene (1992), The South Tibetan detachment system, Himalayan orogen: Extension contemporaneous with and parallel to shortening in a collisional mountain belt, *Geol. Soc. Am., Spec. Pap.*, *269*, 41.

Carosi, R., C. Montomoli, D. Rubatto, and D. Visona (2006), *Channel Flow, Ductile Extrusion and Exhumation in Continental Collision Zones*, edited by R. Law, M. Searle, and L. Godin, *Geol. Soc. London, Spec. Publ.*, *268*, 425–444.

Catlos, E. J., C. S. Dubey, T. M. Harrison, and M. A. Edwards (2004), Late Miocene movement within the Himalayan Main Central Thrust shear zone, Sikkim, north-east India, *J. Metamorph. Geol.*, *22*, 207–226, doi:10.1111/j.1525-1314.2004.00509.x.

Chambers, J., R. Parrish, T. Argles, N. Harris, and M. Horstwood (2011), A short duration pulse of ductile normal shear on the outer South Tibetan detachment in Bhutan: Alternating channel flow and critical taper mechanics of the eastern Himalaya, *Tectonics*, *30*, TC2005, doi:10.1029/2010TC002784.

Chew, D. M., P. J. Sylvester, and M. N. Tubrett (2011), U-Pb and Th-Pb dating of apatite by LA-ICPMS, *Chem. Geol.*, *280*(1–2), 200–216, doi:10.1016/j.chemgeo.2010.11.010.

Coleman, M., and K. Hodges (1995), Evidence for Tibetan plateau uplift before 14 Myr ago from a new minimum age for east-west extension, *Nature*, *374*, 49–52.

Cooper, F. J., B. A. Adams, C. S. Edwards, and K. V. Hodges (2012), Large normal-sense displacement on the South Tibetan fault system in the eastern Himalaya, *Geology*, doi:10.1130/G33318.1.

Cooper, F. J., K. V. Hodges, and B. A. Adams (2013), Metamorphic constraints on the character and displacement of the South Tibetan fault system, central Bhutanese Himalaya, *Lithosphere*, *5*(1), 67–81, doi:10.1130/L221.1.

Corrie, S. L., M. J. Kohn, N. McQuarrie, and S. P. Long (2012), Flattening the Bhutan Himalaya, *Earth Planet. Sci. Lett.*, *349–350*, 67–74, doi:10.1016/j.epsl.2012.07.001.

Cottle, J. M., M. J. Jessup, D. L. Newell, M. S. A. Horstwood, S. R. Noble, R. R. Parrish, D. J. Waters, and M. P. Searle (2009), Geochronology of granulitized eclogite from the Ama Drime Massif: Implications for the tectonic evolution of the South Tibetan Himalaya, *Tectonics*, *28*, TC1002, doi:10.1029/2008TC002256.

Davidson, C., D. E. Grujic, L. S. Hollister, and M. Schmid (1997), Metamorphic reactions related to decompression and synkinematic intrusion of leucogranite, High Himalayan Crystallines, Bhutan, *J. Metamorph. Geol.*, *15*, 593–612.

Dewane, T. J., D. F. Stockli, C. Hager, M. Taylor, L. Ding, J. Lee, and S. Wallis (2006), Timing of Cenozoic E-W extension in the Tangra Yum Co-Kung Co rift, south-central Tibet, *Eos Trans. AGU*, *87*(52), Fall Meeting abstract T34C-04.

Drukpa, D., A. A. Velasco, and D. I. Doser (2006), Seismicity in the Kingdom of Bhutan (1937–2003): Evidence for crustal transcurrent deformation, *J. Geophys. Res.*, *111*, B06301, doi:10.1029/2004JB003087.

Edwards, M. A., and T. M. Harrison (1997), When did the roof collapse? Late Miocene north-south extension in the high Himalaya revealed by Th-Pb monazite dating of the Khula Kangri granite, *Geology*, *25*(6), 543–546.

England, P., and G. Houseman (1989), Extension during continental convergence with application to the Tibetan Plateau, *J. Geophys. Res.*, *94*(B12), 17,561–517,579, doi:10.1029/JB094iB12p17561.

Foster, G. L., H. D. Gibson, R. R. Parrish, M. S. A. Horstwood, J. Fraser, and A. Tindle (2002), Textural, chemical and isotopic insights into the nature and behaviour of metamorphic monazite, *Chem. Geol.*, *191*, 183–207.

Gan, W., P. Zhang, Z.-K. Shen, Z. Niu, M. Wang, Y. Wan, D. Zhou, and J. Cheng (2007), Present-day crustal motion within the Tibetan Plateau inferred from GPS measurements, *J. Geophys. Res.*, *112*, B08416, doi:10.1029/2005JB004120.

Gansser, A. (1983), *Geology of the Bhutan Himalaya*, 181 pp., Birkhauser Verlag, Basel.

Gibson, H. D., S. D. Carr, R. L. Brown, and M. A. Hamilton (2004), Correlations between chemical and age domains in monazite, and metamorphic reactions involving major pelitic phases: An integration of ID-TIMS and SHRIMP geochronology with Y-Th-U X-ray mapping, *Chem. Geol.*, *211*, 237–260, doi:10.1016/j.chemgeo.2004.06.028.

Gordon, S. M., M. Grove, D. L. Whitney, A. K. Schmitt, and C. Teyssier (2009), Time-temperature-fluid evolution of migmatite dome crystallization: Coupled U-Pb age, Ti thermometry, and O isotopic ion microprobe depth profiling of zircon and monazite, *Chem. Geol.*, *262*, 186–201.

Groppo, C., D. Rubatto, F. Rolfo, and B. Lombardo (2010), Early Oligocene partial melting in the Main Central Thrust Zone (Arun valley, eastern Nepal Himalaya), *Lithos*, *118*(3–4), 287–301, doi:10.1016/j.lithos.2010.05.003.

Groppo, C., F. Rolfo, and A. Indares (2012), Partial melting in the Higher Himalayan Crystallines of Eastern Nepal: The effect of decompression and implications for the "channel flow" model, *J. Petrol.*, *53*(5), 1057–1088, doi:10.1093/petrology/egs009.

Grujic, D., L. S. Hollister, and R. R. Parrish (2002), Himalayan metamorphic sequence as an orogenic channel: Insight from Bhutan, *Earth Planet. Sci. Lett.*, *198*, 177–191.

Grujic, D., C. J. Warren, and J. L. Wooden (2011), Rapid synconvergent exhumation of Miocene-aged lower orogenic crust in the eastern Himalaya, *Lithosphere*, *3*(5), 346–366.

Guillot, S., K. V. Hodges, P. Le Fort, and A. Pêcher (1994), New constraints on the age of the Manaslu leucogranite: Evidence for episodic tectonic denudation in the central Himalayas, *Geology*, *22*, 559–562.

Hager, C., D. F. Stockli, T. J. Dewane, G. Gehrels, and L. Ding (2009), Anatomy and crustal evolution of the central Lhasa terrane (S-Tibet) revealed by investigations in the Xainza rift, *Geophysical Research Abstracts*, *EGU General Assembly*, *11*, EGU2009-11346-11341.

Harris, N., and J. Massey (1994), Decompression and anatexis of Himalayan metapelites, *Tectonics*, *13*(6), 1537–1546, doi:10.1029/94TC01611.

Harrison, T. M., P. Copeland, and O. M. Lovera (1995a), Activation of the Nyainqentanghla Shear Zone: Implications for uplift of the southern Tibetan Plateau, *Tectonics*, *14*(3), 658–676, doi:10.1029/95TC00608.

Harrison, T. M., K. I. Mahon, S. Guillot, K. Hodges, P. Le Fort, and A. Pêcher (1995b), New constraints on the age of the Manaslu leucogranite: Evidence for episodic tectonic denudation in the central Himalaya: Comment and reply, *Geology*, *23*, 478–480.

Harrison, T. M., M. Grove, K. D. McKeegan, C. D. Coath, O. M. Lovera, and P. LeFort (1999), Origin and episodic emplacement of the Manaslu Intrusive Complex, Central Himalaya, *J. Petrol.*, *40*, 3–19.

Hauck, M. L., K. D. Nelson, L. D. Brown, W. Zhao, and A. R. Ross (1998), Crustal structure of the Himalayan orogen at ~90° east longitude from Project INDEPTH deep reflection profiles, *Tectonics*, *17*(4), 481–500, doi:10.1029/98TC01314.

Hintersberger, E., R. C. Thiede, M. R. Strecker, and B. R. Hacker (2010), East-west extension in the NW Indian Himalaya, *Geol. Soc. Am. Bull.*, *122*(9/10), 1499–1515, doi:10.1130/B26589.1.

Hodges, K. V. (2000), Tectonics of the Himalaya and southern Tibet from two perspectives, *Geol. Soc. Am. Bull.*, *112*(3), 324–350.

Hodges, K. V., M. S. Hubbard, and D. S. Silverberg (1988), Metamorphic constraints on the thermal evolution of the central Himalayan orogen, *Philos. Trans. R. Soc. London*, *326*, 257–280.

Hodges, K. V., R. R. Parrish, and M. P. Searle (1996), Tectonic evolution of the central Annapurna Range, Nepalese Himalayas, *Tectonics*, *15*(6), 1264–1291, doi:10.1029/96TC01791.

Hodges, K., R. Parrish, T. Housh, D. Lux, B. Burchfiel, L. Royden, and Z. Chen (1992), Simultaneous Miocene extension and shortening in the Himalayan orogen, *Science*, *258*, 1466–1470.

Hodges, K., J. Hurtado, and K. Whipple (2001), Southward extrusion of Tibetan crust and its effect on Himalayan tectonics, *Tectonics*, *20*(6), 799–809, doi:10.1029/2001TC001281.

Hollister, L. S., and D. Grujic (2006), Pulsed channel flow in Bhutan, in *Channel Flow, Ductile Extrusion and Exhumation in Continental Collision Zones*, *Geol. Soc. London, Spec. Publ.*, edited by R. Law, M. Searle, and L. Godin, pp. 415–423, Geol. Soc., London.

Hurtado, J., K. Hodges, and K. Whipple (2001), Neotectonics of the Thakkhola graben and implications for recent activity on the South Tibetan fault system in the central Nepal Himalaya, *Geol. Soc. Am. Bull.*, *113*(2), 222–240.

Imayama, T., et al. (2012), Two-stage partial melting and contrasting cooling history within the Higher Himalayan Crystalline Sequence in the far-eastern Nepal Himalaya, *Lithos*, *134–135*, 1–22, doi:10.1016/j.lithos.2011.12.004.

Jackson, S. E., N. J. Pearson, W. L. Griffin, and E. A. Belousova (2004), The application of laser ablation-inductively coupled plasma-mass spectrometry to in situ U-Pb zircon geochronology, *Chem. Geol.*, *211*, 47–69, doi:10.1016/j.chemgeo.2004.06.017.

Jangpangi, B. S. (1974), Stratigraphy and tectonics of parts of eastern Bhutan, *Himalayan Geol.*, *4*, 139–147.

Jessup, M. J., D. L. Newell, J. M. Cottle, A. L. Berger, and J. A. Spotila (2008), Orogen-parallel extension and exhumation enhanced by denudation in the trans-Himalayan Arun River gorge, Ama Drime Massif, Tibet-Nepal, *Geology*, *36*(7), 587–590, doi:10.1130/G24722A.1.

Kali, E., P. H. Leloup, N. Arnaud, G. Maheo, D. Liu, E. Boutonnet, J. Van der Woerd, X. Liu, J. Liu-Zeng, and H. Li (2010), Exhumation history of the deepest central Himalayan rocks, Ama Drime range: Key pressure-temperature-deformation-time constraints on orogenic models, *Tectonics*, *29*, TC2014, doi:10.1029/2009TC002551.

Kapp, P. A., and A. Yin (2001), Unbending of the lithosphere as a mechanism for active rifting in Tibet: Insight from elastic modelling, *Eos Trans. AGU*, *82*(47), Fall Meet. Suppl., Abstract T11E-0893.

Kellett, D. A., and D. Grujic (2012), New insight into the South Tibetan detachment system: Not a single progressive deformation, *Tectonics*, *31*, TC2007, doi:10.1029/2011TC002957.

Kellett, D. A., D. Grujic, I. Coutand, J. Cottle, and M. Mukul (2013), The South Tibetan detachment system facilitates ultra rapid cooling of granulite-facies rocks in Sikkim Himalaya, *Tectonics*, *32*, 252–270, doi:10.1002/tect.20014.

Kellett, D., D. Grujic, and S. Erdmann (2009), Miocene structural reorganization of the South Tibetan detachment, eastern Himalaya: Implications for continental collision, *Lithosphere*, *1*(5), 259–281.

Kellett, D., D. Grujic, C. Warren, J. Cottle, R. Jamieson, and T. Tenzin (2010), Metamorphic history of a syn-convergent orogen-parallel detachment: The South Tibetan detachment system, Bhutan Himalaya, *J. Metamorph. Geol.*, doi:10.1111/j.1525-1314.2010.00893.x.

Kelly, N. M., S. L. Harley, and A. Möller (2012), Complexity in the behavior and recrystallization of monazite during high-T metamorphism and fluid infiltration, *Chem. Geol.*, *322–323*, 192–208, doi:10.1016/j.chemgeo.2012.07.001.

Kohn, M. J. (2008), P-T-t data from central Nepal support critical taper and repudiate large-scale channel flow of the Greater Himalayan Sequence, *Geol. Soc. Am. Bull.*, *120*, 259–273, doi:10.1130/B26252.1.

Law, R. D., M. J. Jessup, M. P. Searle, M. K. Francsis, D. J. Waters, and J. M. Cottle (2011), Telescoping of isotherms beneath the South Tibetan Detachment System, Mount Everest Massif, *J. Struct. Geol.*, *33*, 1569–1594, doi:10.1016/j.jsg.2011.09.004.

Le Fort, P., M. Cuney, C. Deniel, C. France-Lanord, S. M. F. Sheppard, B. N. Upreti, and P. Vidal (1987), Crustal generation of the Himalayan leucogranites, *Tectonophysics*, *134*(1–3), 39–57, doi:10.1016/0040-1951(87)90248-4.

Lederer, G. W., J. M. Cottle, M. J. Jessup, J. M. Langille, and T. Ahmad (2013), Timescales of partial melting in the Himalayan middle crust: Insight from the Leo Pargil dome, northwest India, *Contrib. Mineral. Petrol.*, *166*, 1415–1441, doi:10.1007/s00410-013-0935-9.

Lee, J., C. Hager, S. R. Wallis, D. F. Stockli, M. J. Whitehouse, M. Aoya, and Y. Wang (2011), Middle to late Miocene extremely rapid exhumation and thermal reequilibration in the Kung Co rift, southern Tibet, *Tectonics*, *30*, TC2007, doi:10.1029/2010TC002745.

Long, S., and N. McQuarrie (2010), Placing limits on channel flow: Insights from the Bhutan Himalaya, *Earth Planet. Sci. Lett.*, *290*, 375–390.

Long, S. P., N. McQuarrie, T. Tobgay, D. Grujic, and L. Hollister (2011), Geologic map of Bhutan, *J. Maps*, *2011*, 184–192, doi:10.4113/jom.2011.1159.

Ludwig, K. R. (2003), *User's Manual for Isoplot 3.00: A Geochronological Toolkit for Microsoft Excel*, Berkeley Geochronological Center, Berkeley, Calif.

Maheo, G., P. H. Leloup, F. Valli, R. Lacassin, N. Arnaud, J.-L. Paquette, A. Fernandez, L. Haibing, K. A. Farley, and P. Tapponnier (2007), Post 4 Ma initiation of normal faulting in southern Tibet. Constraints from the Kung Co half graben, *Earth Planet. Sci. Lett.*, *256*, 233–243, doi:10.1016/j.epsl.2007.01.029.

McCaffrey, R. (1996), Estimates of modern arc-parallel strain rates in fore-arcs, *Geology*, *24*(1), 27–30, doi:10.1130/0091-7613(1996)024<0027:EOMAPS>2.3.CO;2.

McCaffrey, R., and J. Nabelek (1998), Role of oblique convergence in the active deformation of the Himalayas and southern Tibet Plateau, *Geology*, *26*, 691–694, doi:10.1130/0091-7613(1998)026<0691:ROOCIT>2.3.CO;2.

McDermott, J. A., K. X. Whipple, K. V. Hodges, and M. C. van Soest (2013), Evidence for Plio-Pleistocene north–south extension at the southern margin of the Tibetan Plateau, Nyalam region, *Tectonics*, *32*, 1–17, doi:10.1002/tect.20018.

McDermott, J. A., K. V. Hodges, K. X. Whipple, M. C. van Soest, and J. M. Hurtado (2015), Evidence for Pleistocene low-angle normal faulting in the Annapurna-Dhaulagiri Region, Nepal, *J. Geol.*, *123*(2), 133–151, doi:10.1086/681219.

Meyer, M. C., G. Wiesmayr, M. Brauner, H. Häusler, and D. Wangda (2006), Active tectonics in Eastern Lunana (NW Bhutan): Implications for the seismic and glacial hazard potential of the Bhutan Himalaya, *Tectonics*, *25*, TC3001, doi:10.1029/2005TC001858.

Mitsuishi, M., S. R. Wallis, M. Aoya, J. Lee, and Y. Wang (2012), E-W extension at 19 Ma in the Kung Co area, S. Tibet: Evidence for contemporaneous E-W and N-S extension in the Himalayan orogen, *Earth Planet. Sci. Lett.*, *325–326*, 10–20, doi:10.1016/j.epsl.2011.11.013.

Molnar, P., and W. P. Chen (1983), Focal depths and fault plane solutions of earthquakes under the Tibetan Plateau, *J. Geophys. Res.*, *88*(B2), 1180–1196, doi:10.1029/JB088iB02p01180.

Molnar, P., and H. Lyon-Caen (1989), Fault-plane solutions of earthquakes and active tectonics of the Tibetan Plateau and its margins, *Geophys. J. Int.*, *99*(1), 123–153, doi:10.1111/j.1365-246X.1989.tb02020.x.

Molnar, P., and P. Tapponnier (1975), Cenozoic tectonics of Asia: Effects of a continental collision, *Science*, *189*, 419–426.

Molnar, P., and P. Tapponnier (1978), Active tectonics of Tibet, *J. Geophys. Res.*, *83*, 5361–5375, doi:10.1029/JB083iB11p05361.

Murphy, M. A. (2007), Isotopic characteristics of the Gurla Mandhata metamorphic core complex: Implications for the architecture of the Himalayan orogen, *Geology*, *35*(11), 983–986, doi:10.1130/G23774A.1.

Murphy, M. A., and P. Copeland (2005), Transtensional deformation in the central Himalaya and its role in accommodating growth of the Himalayan orogen, *Tectonics*, *24*, TC4012, doi:10.1029/2004TC001659.

Murphy, M. A., and M. T. Harrison (1999), Relationship between leucogranites and the Qomolangma detachment in the Rongbuk Valley, south Tibet, *Geology*, *27*(9), 831–834.

Murphy, M. A., A. Yin, P. Kapp, T. M. Harrison, C. E. Manning, F. J. Ryerson, D. Lin, and G. Jinghui (2002), Structural evolution of the Gurla Mandhata detachment system, southwest Tibet: Implications for the eastward extent of the Karakoram fault system, *Geol. Soc. Am. Bull.*, *114*(4), 428–447.

Nautiyal, S. P., B. S. Jangpangi, P. Singh, T. K. Guha Sarkar, V. D. Bhate, M. R. Raghavan, and T. N. Sahai (1964), A preliminary note on the geology of the Bhutan Himalaya, *Report of the 22nd International Geologic Congress*, *New Delhi*, *11*, 1–14.

Nelson, K. D., et al. (1996), Partially molten middle crust beneath southern Tibet: Synthesis of Project INDEPTH Results, *Science*, *274*, 1684–1688.

Palin, R. M., M. P. Searle, D. J. Waters, R. R. Parrish, N. M. W. Roberts, M. S. A. Horstwood, M.-W. Yeh, S.-L. Chung, and T. T. Anh (2013), A geochronological and petrological study of anatectic paragneiss and associated granite dykes from the Day Nui Con Voi metamorphic core complex, North Vietnam: Constraints on the timing of metamorphism within the Red River shear zone, *J. Metamorph. Geol.*, *31*, 359–387, doi:10.1111/jmg.12025.

Ratschbacher, L., W. Frisch, G. H. Liu, and C. S. Chen (1994), Distributed deformation in southern and western Tibet during and after the India-Asia collision, *J. Geophys. Res.*, *99*(B10), 19,917–19,945, doi:10.1029/94JB00932.

Ratschbacher, L., I. Krumrei, M. Blumenwitz, M. Staiger, R. Gloaguen, B. V. Miller, S. D. Samson, M. A. Edwards, and E. Appel (2011), Rifting and strike-slip shear in central Tibet and the geometry, age and kinematics of upper crustal extension in Tibet, *Geol. Soc. London, Spec. Publ.*, *353*, 127–163, doi:10.1144/SP353.8.

Regis, D., C. J. Warren, D. Young, and N. M. W. Roberts (2014), Tectono-metamorphic evolution of the Jomolhari massif: Variations in timing of syn-collisional metamorphism across western Bhutan, *Lithos*, *190–191*, 449–466, doi:10.1016/j.lithos.2014.01.001.

Robinson, A. C., A. Yin, C. E. Manning, T. M. Harrison, S. Zhang, and X. Wang (2007), Cenozoic evolution of the eastern Pamir: Implications for strain accommodation mechanisms at the western end of the Himalayan-Tibetan orogen, *Geol. Soc. Am. Bull.*, *119*(7/8), 882–896, doi:10.1130/B25981.1.

Royden, L. H., and B. C. Burchfiel (1987), Thin-skinned north–south extension within the convergent Himalayan region: Gravitational collapse of a Miocene topographic front, in *Continental Extensional Tectonics*, *Geol. Soc. London Spec. Publ.*, vol. 28, edited by M. P. Coward, J. F. Dewey, and P. L. Hancock, pp. 611–619, Geol. Soc., London.

Rubatto, D., S. Chakraborty, and S. Dasgupta (2013), Timescales of crustal melting in the Higher Himalayan Crystallines (Sikkim, Eastern Himalaya) inferred from trace element-constrained monazite and zircon chronology, *Contrib. Mineral. Petrol.*, *165*(2), 349–372.

Schoene, B., J. L. Crowley, D. J. Condon, M. D. Schmitz, and S. A. Bowring (2006), Reassessing the uranium decay constants for geochronology using ID-TIMS U-Pb data, *Geochim. Cosmochim. Acta*, *70*, 426–445, doi:10.1016/j.gca.2005.09.007.

Searle, M. P., S. R. Noble, A. J. Hurford, and D. C. Rex (1999), Age of crustal melting, emplacement and exhumation history of the Shivling leucogranite, Garhwal Himalaya, *Geol. Mag.*, *136*(5), 513–525.

Searle, M., R. Parrish, K. Hodges, A. Hurford, M. Ayers, and M. Whitehouse (1997), Shisha Pangma leucogranite, South Tibetan Himalaya: Field relations, geochemistry, age, origin, and emplacement, *J. Geol.*, *105*, 295–317.

Seeber, L., and J. Armbruster (1984), Some elements of continental subduction along the Himalayan front, *Tectonophysics*, *105*, 263–278, doi:10.1016/0040-1951(84)90207-5.

Sláma, J., et al. (2008), Plešovice zircon—A new natural reference material for U-Pb and Hf isotopic microanalysis, *Chem. Geol.*, *249*, 1–35.

Stacey, J. S., and J. D. Kramers (1975), Approximation of terrestrial lead isotope evolution by a two-stage model, *Earth Planet. Sci. Lett.*, *26*(2), 207–221, doi:10.1016/0012-821X(75)90088-6.

Stockli, D. F., M. Taylor, T. M. Harrison, J. D'Andrea, P. Kapp, and D. Lin (2002), Late Miocene-Pliocene inception of E-W extension in Tibet as evidenced by apatite (U-Th)/He data, *Geological Society of America Abstract 182–8*.

Swapp, S. M., and L. S. Hollister (1991), Inverted metamorphism within the Tibetan slab of Bhutan: Evidence for a tectonically transported heat-source, *Can. Mineral.*, *29*, 1019–1041.

Tangri, S. K., and A. C. Pande (1995), Tethyan Sequence, in *The Bhutan Himalaya: A Geological Account*, edited by O. N. Bhargava, pp. 109–141, Geological Survey of India, Calcutta.

Tapponnier, P., G. Peltzer, A. Ledain, R. Armijo, and P. Cobbold (1982), Propagating extrusion tectonics in Asia: New insights from simple experiments with plasticine, *Geology*, *10*(12), 611–616, doi:10.1130/0091-7613(1982)10<611:PETIAN>2.0.CO;2.

Taylor, M., and A. Yin (2009), Active structures of the Himalayan-Tibetan orogen and their relationships to earthquake distribution, contemporary strain field, and Cenozoic volcanism, *Geosphere*, *5*(3), 199–214, doi:10.1130/GES00217.1.

Taylor, M., A. Yin, F. J. Ryerson, P. Kapp, and L. Ding (2003), Conjugate strike-slip faulting along the Bangong-Nujiang suture zone accommodates coeval east–west extension and north–south shortening in the interior of the Tibetan Plateau, *Tectonics*, *22*(4), 1044, doi:10.1029/2002TC001361.

Thiede, R. C., J. R. Arrowsmith, B. Bookhagen, M. McWilliams, E. R. Sobel, and M. R. Strecker (2006), Dome formation and extension in the Tethyan Himalaya, Leo Pargil, northwest India, *Geol. Soc. Am. Bull.*, *118*(5/6), 635–650, doi:10.1130/B25872.1.

Tobgay, T., N. McQuarrie, S. Long, M. J. Kohn, and S. L. Corrie (2012), The age and rate of displacement along the Main Central Thrust in the western Bhutan Himalaya, *Earth Planet. Sci. Lett.*, *319–320*, 146–158.

Tseng, T. L., W. P. Chen, and R. L. Nowack (2009), Northward thinning of Tibetan crust revealed by virtual seismic profiles, *Geophys. Res. Lett.*, *36*, L24304, doi:10.1029/2009GL040457.

Vannay, J.-C., B. Grasemann, M. Rahn, W. Frank, A. Carter, V. Baudraz, and M. Cosca (2004), Miocene to Holocene exhumation of metamorphic crustal wedges in the NW Himalaya: Evidence for tectonic extrusion coupled to fluvial erosion, *Tectonics*, *23*, TC1014, doi:10.1029/2002TC001429.

Viskupic, K., K. V. Hodges, and S. A. Bowring (2005), Timescales of melt generation and the thermal evolution of the Himalayan metamorphic core, Everest region, eastern Nepal, *Contrib. Mineral. Petrol.*, *149*, 1–21, doi:10.1007/s00410-004-0628-5.

Walker, J. D., M. W. Martin, S. A. Bowring, M. P. Searle, D. J. Waters, and K. V. Hodges (1999), Metamorphism, melting, and extension: Age constraints from the High Himalayan slab of southeast Zanskar and northwest Lahaul, *J. Geol.*, *107*, 473–495.

Warren, C. J., D. Grujic, D. A. Kellett, J. Cottle, R. A. Jamieson, and K. S. Ghalley (2011), Probing the depths of the India-Asia collision: U-Th-Pb monazite chronology of granulites from NW Bhutan, *Tectonics*, *30*, TC2004, doi:10.1029/2010TC002738.

Webb, A. A. G., A. Yin, T. M. Harrison, J. Célérier, and W. P. Burgess (2007), The leading edge of the Greater Himalayan Crystallines revealed in the NW Indian Himalaya: Implications for the evolution of the Himalayan orogen, *Geology*, *35*, 955–958, doi:10.1130/G23931A.1.

Webb, A. A. G., A. Yin, and C. S. Dubey (2013), U-Pb zircon geochronology of major lithologic units in the eastern Himalaya: Implications for the origin and assembly of Himalayan rocks, *Geol. Soc. Am. Bull.*, *125*(3/4), 499–522, doi:10.1130/B30626.1.

Whipp, D. M., C. Beaumont, and J. Braun (2014), Orogen-parallel mass transport into Nanga Parbat and the western Himalayan syntaxis, *J. Geophys. Res. Solid Earth*, *119*, 5077–5096, doi:10.1002/2013JB010929.

Wiesmayr, G., M. A. Edwards, M. Meyer, W. S. F. Kidd, D. Leber, H. Häusler, and D. Wangda (2002), Evidence for steady fault-accommodated strain in the High Himalaya: Progressive fault rotation of the southern Tibet detachment system in NW Bhutan, in *Deformation Mechanisms, Rheology and Tectonics: Current Status and Future Perspectives*, edited by S. De Meer et al., pp. 371–386, Geol. Soc., London.

Williams, H., S. Turner, S. Kelley, and N. Harris (2001), Age and composition of dikes in Southern Tibet: New constraints on the timing of east–west extension and its relationship to postcollisional volcanism, *Geology*, *29*(4), 339–342.

Wu, C., K. D. Nelson, G. Wortman, S. D. Samson, Y. Yue, J. Li, W. S. F. Kidd, and M. A. Edwards (1998), Yadong cross structure and South Tibetan Detachment in the east central Himalaya (89–90°E), *Tectonics*, *17*(1), 28–45, doi:10.1029/97TC03386.

Wu, Z.-H., P.-S. Ye, P. J. Barosh, and Z.-H. Wu (2011), The October 6, 2008 M_w 6.3 magnitude Damxung earthquake, Yadong-Gulu rift, Tibet, and implications for present-day crustal deformation within Tibet, *J. Asian Earth Sci.*, *40*, 943–957, doi:10.1016/j.jseaes.2010.05.003.

Yin, A. (2006), Cenozoic tectonic evolution of the Himalayan orogen as constrained by along-strike variation of structural geometry, exhumation history, and foreland sedimentation, *Earth Sci. Rev.*, *76*, 1–131.

Yin, A., T. M. Harrison, F. J. Ryerson, W. Chen, W. S. F. Kidd, and P. Copeland (1994), Tertiary structural evolution of the Gangdese thrust system, southeastern Tibet, *J. Geophys. Res.*, *99*, 18,175–18,201, doi:10.1029/94JB00504.

Yin, A., T. M. Harrison, M. A. Murphy, M. Grove, S. Nie, F. J. Ryerson, W. X. Feng, and C. Z. Le (1999), Tertiary deformation history of southeastern and southwestern Tibet during the Indo-Asian collision, *Geol. Soc. Am. Bull.*, *111*(11), 1644–1664.

Zhang, J., and L. Guo (2007), Structure and geochronology of the southern Xainza-Dinggye rift and its relationship to the south Tibetan detachment system, *J. Asian Earth Sci.*, *29*, 722–736, doi:10.1016/j.jseaes.2006.05.003.

Zhang, P.-Z., et al. (2004), Continuous deformation of the Tibetan Plateau from global positioning system data, *Geology*, *32*(9), 809–812, doi:10.1130/G20554.1.